Author Manuscript

Author Manuscript

Author Manuscript

Author Manuscript

HHS Public Access

Author manuscript

Neuron. Author manuscript; available in PMC 2024 February 15.

Published in final edited form as:

Neuron. 2023 February 15; 111(4): 493–507.e6. doi:10.1016/j.neuron.2022.11.017.

Decreasing Mutant ATXN1 Nuclear Localization Improves a Spectrum of SCA1-Like Phenotypes and Brain Region Transcriptomic Profiles

Hillary P. Handler[1,2], **Lisa Duvick**[1,3], **Jason S. Mitchell**[1,3], **Marija Cvetanovic**[1,2], **Molly Reighard**[1,3], **Alyssa Soles**[1,2], **Kathleen B. Mather**[1,2], **Orion Rainwater**[1,3], **Shannah Serres**[1,3], **Tessa Nichols-Meade**[1,2], **Stephanie L. Coffin**[4], **Yun You**[5], **Brian L. Ruis**[6], **Brennon O'Callaghan**[1,3], **Christine Henzler**[7], **Huda Y. Zoghbi**[8], **Harry T. Orr**[1,3,#]

[1]Institute of Translational Neuroscience, University of Minnesota, Minneapolis, MN 55455, USA.

[2]Department of Neuroscience, University of Minnesota, Minneapolis, MN 55455, USA.

[3]Department of Laboratory Medicine and Pathology, University of Minnesota, Minneapolis, MN 55455, USA.

[4]Program in Genetics & Genomics and Department of Molecular and Human Genetics, Baylor College of Medicine, Jan and Dan Duncan Neurological Research Institute at Texas Children's Hospital, Houston, TX 77030, USA.

[5]Mouse Genetics Laboratory, University of Minnesota, Minneapolis, MN 55455, USA.

[6]Department of Biochemistry, Molecular Biology, and Biophysics, University of Minnesota, Minneapolis, MN 55455, USA.

[7]RISS Bioinformatics, Minnesota Supercomputing Institute, University of Minnesota, Minneapolis, MN 55455, USA.

[8]Departments of Molecular and Human Genetics, Pediatrics, and Howard Hughes Medical Institute, Baylor College of Medicine, Jan and Dan Duncan Neurological Research Institute at Texas Children's Hospital, Houston, TX 77030, USA.

SUMMARY

[#]Lead Contact: orrxx002@umn.edu (HTO).

AUTHOR CONTRIBUTIONS

H.P.H. and H.T.O. conceived the study and wrote the paper. H.P.H., S.L.C., M.C, H.Y.Z, and H.T.O. designed experiments and interpreted the data. H.Y.Z. generated the *Atxn1*$^{154Q/2Q}$ mouse model. B.O. and H.P.H designed the CRISPR-Cas9 strategy used to generate the *Atxn1*$^{175QK772T/2Q}$ mouse model. B.R. assessed the efficacy of the CRISPR-Cas9 strategy in 3T3 cells. Y.Y. performed embryo injections and implantations. O.R. and S.S. bred mice and managed the colony. H.P.H. genotyped mice. H.P.H., O.R., and S.S. conducted the survival study and animal weight measurements. K.B.M. performed DARPP-32 western blot. O.R. and T.N.-M. performed behavioral assays. H.P.H. and B.O. performed subcellular fractionation assays. H.P.H., A.S., and M.R. performed extractability assays. L.D. sectioned and stained tissue for immunofluorescence. J.M. developed and implemented immunofluorescence image analyses. H.P.H. performed statistical analyses. H.P.H. and C.H. performed RNAseq analyses. All authors reviewed the manuscript and provided input.

Publisher's Disclaimer: This is a PDF file of an unedited manuscript that has been accepted for publication. As a service to our customers we are providing this early version of the manuscript. The manuscript will undergo copyediting, typesetting, and review of the resulting proof before it is published in its final form. Please note that during the production process errors may be discovered which could affect the content, and all legal disclaimers that apply to the journal pertain.

DECLARATION OF INTERESTS

The authors declare no competing interests.

Author Manuscript Author Manuscript Author Manuscript Author Manuscript

Spinocerebellar ataxia type 1 (SCA1) is a dominant trinucleotide repeat neurodegenerative disease characterized by motor dysfunction, cognitive impairment, and premature death. Degeneration of cerebellar Purkinje cells is a frequent and prominent pathological feature of SCA1. We previously showed that transport of ATXN1 to Purkinje cell nuclei is required for pathology, where mutant ATXN1 alters transcription. To examine the role of ATXN1 nuclear localization broadly in SCA1-like disease pathogenesis, CRISPR-Cas9 was used to develop a mouse with an amino acid alteration (K772T) in the nuclear localization sequence of the expanded ATXN1 protein. Characterization of these mice indicates proper nuclear localization of mutant ATXN1 contributes to many disease-like phenotypes including motor dysfunction, cognitive deficits, and premature lethality. RNA sequencing analysis of genes with expression corrected to WT levels in $Atxn1^{175QK772T/2Q}$ mice indicates that transcriptomic aspects of SCA1 pathogenesis differ between the cerebellum, brainstem, cerebral cortex, hippocampus, and striatum.

eTOC blurb

SCA1, a lethal polyglutamine (polyQ) neurodegenerative disease, displays motor and cognitive impairments. CRISPR-Cas9 was used to mutate the nuclear localization sequence of ATXN1-polyQ in a knockin SCA1 mouse model. Results indicate ATXN1-polyQ nuclear localization contributes to all SCA1-like phenotypes. Yet, disease-associated changes in gene expression differ between affected brain regions.

Keywords

Spinocerebellar ataxia type 1; SCA1; neurodegeneration; nuclear localization

INTRODUCTION

A challenge facing neurodegenerative disease research is the elucidation of key molecular aspects of pathogenesis. Study of molecular pathogenic pathways has typically focused on a limited number of neuronal types that have been characterized as primary sites of pathogenesis. However, such an approach overlooks two critical points: it is becoming increasingly apparent that many neurodegenerative diseases impact multiple cell types and circuits throughout the brain and critical neuronal dysfunction can occur in absence of overt pathology.

Spinocerebellar ataxia type 1 (SCA1) is one of several inherited neurodegenerative diseases caused by expansion of a glutamine-encoding CAG triplet in the affected gene, *ATXN1* in the case of SCA1.[1] SCA1 is characterized by a progressive loss of motor function along with prominent and consistent degeneration of cerebellar Purkinje neurons. Accordingly, the cerebellum and Purkinje neurons are a major focus of SCA1 research. Our work identified several ATXN1 functional features that have a critical role in SCA1 pathogenesis in Purkinje neurons such as the importance of ATXN1 entry into Purkinje cell nuclei for Purkinje cell pathogenesis.[2] Additionally, presence of nuclear polyQ expanded protein correlates with toxicity for other diseases including Huntington's disease[3]; dentatorubral-pallidoluysian atrophy[4]; and SCA3.[5]

Author Manuscript Author Manuscript Author Manuscript Author Manuscript

As SCA1 progresses, symptoms include muscle wasting, cognitive deficits, and bulbar dysfunction resulting in respiratory complications that are a primary cause of premature lethality.[6-10] Correspondingly, a comprehensive pathological study on SCA1 postmortem brains revealed that, in addition to cerebellar degeneration, there was widespread neuronal loss in the primary motor cortex, basal forebrain, thalamus, and brainstem.[11] Moreover, longitudinal MRI studies on SCA1 patients identified cerebellar atrophy at diagnosis and changes in brainstem, pons, caudate, and putamen with disease progression.[12,13]

To model the totality of SCA1, *Atxn1*$^{154Q/2Q}$ knock-in mice were generated by the insertion of an expanded CAG repeat into one allele of the mouse *Atxn1* gene. These mice express ATXN1[154Q] throughout the brain and display, in addition to ataxia, a range of SCA1-like disease phenotypes including muscle loss, cognitive impairments, and premature lethality.[14] Here, we show that disrupting nuclear localization in knock-in mice by replacing lysine with a threonine at position 772 in the nuclear localization sequence (NLS) of expanded ATXN1, an amino acid change previously shown to block ATXN1[82Q]-induced Purkinje cell disease,[2] dampens all of the SCA1-like symptoms seen in these mice. RNA sequencing (RNAseq) was used as means of comparing the disease process in regions of the brain impacted by SCA1. While proper nuclear localization underlies pathogenesis throughout the brain, RNAseq data indicate that molecular aspects of SCA1 pathogenesis differ among the five regions examined: cerebellum, medulla, cerebral cortex, hippocampus, and striatum.

RESULTS

Introduction of a K772T NLS mutation in ATXN1[175Q] improves SCA1-like disease phenotypes

We previously demonstrated that ATXN1 contains a functional NLS near its C-terminus, spanning residues 771-774, and that mutating the lysine at position 772 to a threonine disrupted nuclear localization of ATXN1 in cerebellar Purkinje cells. Importantly, when the K772T NLS mutation was introduced into a transgenic mouse model with ATXN1[82Q] expressed exclusively by cerebellar Purkinje cells, the animals no longer developed ataxia or signs of Purkinje cell pathology.[2] In this study, CRISPR-Cas9 was used to introduce the ATXN1 K772T NLS alteration to the expanded allele of *Atxn1*$^{154Q/2Q}$ knock-in mice. To achieve this, three nucleotides in the expanded *Atxn1* gene were altered (Figure 1A). Two changes (AG → CC) were required to generate the K772T amino acid alteration and an additional nucleotide change (C → T) served two purposes: 1) ablation of the PAM site to prevent Cas9 from recognizing and cleaving DNA that had already been altered and 2) introduction of an Alu1 restriction enzyme digest site to expedite genotyping of the mice. Integration of the desired genetic alterations in this region of *Atxn1* was confirmed using Sanger sequencing (Figure 1B). Further, Sanger sequencing of the *Atxn1* repeat region was performed for both the existing knock-in line and the new NLS mutant knock-in line. The CAG repeat length was identical in both genotypes, but a germline expansion from 154 repeats to 175 occurred. Accordingly, the knock-in mouse line we used in this study is designated as *Atxn1(175Q)* (*Atxn1*$^{175Q/2Q}$) and the knock-in model with the ATXN1 K772T NLS alteration is designated as *Atxn1(175Q)K772T* (*Atxn1*$^{175QK772T/2Q}$).

Author Manuscript Author Manuscript Author Manuscript Author Manuscript

To establish whether the NLS mutation improves SCA1-like phenotypic deficits historically observed in *Atxn1*$^{154Q/2Q}$ mice, we performed a series of assessments comparing WT, *Atxn1(175Q)K772T,* and *Atxn1(175Q)* mice. One prominent SCA1 phenotype is progressive ataxia and motor decline.[15] Motor performance and coordination was assessed by accelerating rotarod in the same cohort of WT, *Atxn1(175Q)K772T,* and *Atxn1(175Q)* mice periodically between 6 and 24 weeks of age. At each age, mice were assessed using one rotarod trial daily for four consecutive days. On the first trial day at 6 weeks of age, there were no significant differences in performance across the three genotypes of naïve mice (Figure 2A). Between trial day 1 and day 4 at 6 weeks of age, the performance of the WT mice improved significantly ($p=0.0008$) whereas the performance of the *Atxn1(175Q)K772T* and *Atxn1(175Q)* mice did not change significantly (Figure 2A). This indicates that WT mice were able to learn the motor task with training while mice expressing expanded ATXN1 could not.

Trial day 4 performance did not differ significantly for WT or *Atxn1(175Q)K772T* mice between 6 weeks and 24 weeks of age (Figure 2B). In contrast, trial day 4 performance declined significantly ($p<0.0001$) between 6 and 24 weeks of age for *Atxn1(175Q)* mice. When comparing trial day 4 performance across genotypes at a given age, all genotypes were significantly different from all other genotypes at each age assessed except for the comparison between *Atxn1(175Q)K772T* and *Atxn1(175Q)* mice at 6 weeks of age (Figure 2B). These findings indicate that the NLS mutation in the *Atxn1(175Q)K772T* mice mitigates the decline in motor performance and coordination observed with aging in *Atxn1(175Q)* mice.

Studies show that changes occur in neural activity in striatal medium-sized spiny neurons (MSNs) during motor learning.[16-19] Dopamine- and cAMP-regulated phosphoprotein (DARPP-32), a regulator of dopamine receptor signaling, is highly enriched in striatal MSNs.[20] Notably, DARPP-32 levels are decreased in mouse models of Huntington's disease.[21,22] Striatal RNAseq and Western blot data from 10-week-old *Atxn1(175Q)* and *Atxn1(175Q)K772T* mice shows that *Darpp-32* mRNA and DARPP-32 protein expression was significantly reduced compared to WT mice (Figure 3A-C). Additionally, striatal RNAseq data from 10-week-old *Atxn1(175Q)* and *Atxn1(175Q)K772T* mice shows that expression of the dopamine D1 and D2 receptors, key regulators of MSN activity,[23] were decreased (Figure 3D). These results indicate that genes critical for motor learning are similarly altered in both *Atxn1(175Q)* and *Atxn1(175Q)K772T* mice.

To determine if the NLS mutation improved premature lethality observed in *Atxn1*$^{154Q/2Q}$ mice,[14] a survival study was performed on *Atxn1(175Q)* and *Atxn1(175Q)K772T* mice. Median survival of *Atxn1(175Q)* mice was 27.4 weeks, while *Atxn1(175Q)K772T* mice survived significantly longer ($p<0.0001$), with a median lifespan of 49.1 weeks (Figure 2C). Thus, the NLS mutation had a dramatic impact on survival.

Atxn1$^{154Q/2Q}$ mice also display failure to gain weight.[14] To determine if the NLS mutation improved this phenotype, body weight was measured for the same cohort of WT, *Atxn1(175Q)K772T,* and *Atxn1(175Q)* animals periodically between 6 and 24 weeks of age. At 6 weeks of age, there were no significant differences in weight between the

Author Manuscript Author Manuscript Author Manuscript Author Manuscript

three genotypes assessed (Figure 2D). At 12 weeks of age, WT mice weighed significantly more than *Atxn1(175Q)* mice ($p<0.0001$), but there was not a significant difference in weight between WT and *Atxn1(175Q)K772T* mice nor between *Atxn1(175Q)* and *Atxn1(175Q)K772T* mice. At 18 and 24 weeks of age, however, the average weight for each genotype was significantly different from the other two genotypes. Over time, *Atxn1(175Q)* mice displayed a failure to gain weight phenotype: from 6 to 24 weeks of age, there was not a significant difference in body weight among the *Atxn1(175Q)* animals. Both the WT and *Atxn1(175Q)K772T* mice, however, showed a significant increase ($p<0.0001$) in body weight between 6 and 24 weeks of age. Although the weight gain profile of the *Atxn1(175Q)K772T* mice was not as dramatic as that of the WT mice over time, the data indicate that the NLS mutation substantially improves the failure to gain weight phenotype observed in the *Atxn1(175Q)* mice.

As a measure of neurodegeneration, brain weights were assessed for WT, *Atxn1(175Q)K772T,* and *Atxn1(175Q)* mice at 26 weeks of age. Two of the *Atxn1(175Q)* mice were sacrificed at 26 weeks of age and the other two *Atxn1(175Q)* mice were designated moribund by veterinary technicians at 23 weeks of age, requiring euthanasia. Brain weight for each genotype was significantly different from the other genotypes. The NLS mutation significantly mitigates the decreased brain weight observed in *Atxn1(175Q)* mice, but it does not restore brain weight of *Atxn1(175Q)K772T* mice to that of WT mice (Figure 2E).

Since cognitive dysfunctions are seen in some SCA1 patients[24] and *Atxn1*$^{154Q/2Q}$ mice display cognitive deficits,[14,25] we evaluated the cognitive function of WT, *Atxn1(175Q)K772T,* and *Atxn1(175Q)* mice. The Barnes maze assessment, in which mice are placed on a platform where they use visual cues to locate an escape chamber and exit the arena, was used to compare visuospatial learning, memory, and cognitive strategy in the same cohort of mice at 7 and 17 weeks of age (Figure S1). The Barnes-maze unbiased strategy (BUNS) algorithm was used to classify search strategies and score cognitive performance for each animal.[26] At 7 weeks of age, *Atxn1(175Q)K772T* and *Atxn1(175Q)* mice had similar lower cognitive scores compared to WT mice (Figure 2F). By 17 weeks of age, both WT and *Atxn1(175Q)K772T* mice had significantly higher cognitive scores than *Atxn1(175Q)* mice (Figure 2G). These results indicate that *Atxn1(175Q)K772T* mice show improved cognition compared to *Atxn1(175Q)* mice, and although *Atxn1(175Q)K772T* mice did not perform as well as WT mice over time, they were more capable of learning and strategy development than *Atxn1(175Q)* mice. Accordingly, the NLS mutation confers considerable protection against cognitive decline.

Another behavioral measure of cognitive performance used was the contextual fear conditioning assay. Mice were given a series of five foot shocks in an environment with unique visual and olfactory cues. After 24-hours in their home cage, mice were placed into the same environment where shocks were administered and the amount of time spent freezing was measured as an indication of fear associated with the expectation of receiving a foot shock. This assessment was performed with WT, *Atxn1(175Q)K772T,* and *Atxn1(175Q)* mice at 8 weeks of age (Figure 2H). There was no significant difference in fear response between the WT and *Atxn1(175Q)K772T* mice. Both WT and

Author Manuscript Author Manuscript Author Manuscript Author Manuscript

Atxn1(175Q)K772T mice spent a significantly larger proportion of their time freezing than *Atxn1(175Q)* mice. This result further supports the idea that the NLS mutation protects against cognitive deficits, including associative memory.

The K772T ATXN1[175Q] NLS mutation reduces nuclear localization, improves solubility, and alters formation of nuclear inclusions of expanded ATXN1 throughout the brain

We evaluated the impact of the NLS mutation on nuclear entry of expanded ATXN1 protein throughout the brain by assessing the subcellular localization, extractability, and nuclear inclusion formation of ATXN1[175Q] and ATXN1[175Q]K772T from *Atxn1(175Q)* mice and *Atxn1(175Q)K772T* mice. To quantify the relative proportions of ATXN1 in the nucleus and cytoplasm, subcellular fractionation was performed on cerebellum, medulla, cerebral cortex, hippocampus, and striatum tissue (Figure 4 and Figure S2). Of note, the proportion of ATXN1[2Q] in the nucleus was constant across brain region, age, and genotype (average=0.87; range=0.75-0.93). In comparing *Atxn1(175Q)* and *Atxn1(175Q)K772T* mice at 5 weeks of age, there was a significantly higher proportion of ATXN1[175Q] in the nucleus than ATXN1[175Q]K772T for all brain regions assessed. Since quantification of expanded ATXN1 protein quickly becomes less reliable with age,[14] subcellular fractionation was not performed on *Atxn1(175Q)* animals at a later age. In *Atxn1(175Q)K772T* mice, where the extractability of expanded ATXN1[175Q] is much improved (Figure S3 and Figure S4), there was no significant change in the nuclear proportion of ATXN1[175Q]K772T between 5 and 40-42 weeks of age for the medulla, cortex, striatum, and hippocampus (Figure 4). These findings show that the NLS mutation, while not completely preventing nuclear entry, significantly reduces nuclear localization of expanded ATXN1 throughout the brain and across the lifespan of *Atxn1(175Q)K772T* mice.

As noted above, extractability of ATXN1[154Q] decreased rapidly with age, i.e. between 2 and 9 weeks of age in $Atxn1^{154Q/2Q}$ mice.[14] In whole-region extracts from cerebellum, medulla (Figure S3), cortex, hippocampus, and striatum (Figure S4), ATXN1[175Q]K772T was significantly more extractable than ATXN1[175Q] (relative to ATXN1[2Q]) at both 5 and 26 weeks of age. From 5 to 26 weeks, extractability of ATXN1[175Q] did not change significantly in any brain region except the cerebellum, in which extractability decreased over time. While the extractability of ATXN1[175Q]K772T was much greater than that of ATXN1[175Q] in all brain regions assessed at both time points, ATXN1[175Q]K772T did become less extractable over time. For both the extraction blots and the subcellular fractionation blots at 5 weeks of age, the total amount of soluble ATXN1[175Q]K772T was greater than or equal to the level of ATXN1[175Q] in all brain regions assessed (Figure S5). This indicates that, although quantification of expanded ATXN1 is complicated by a reduction in extractability with age, *Atxn1(175Q)K772T* mice express mutant protein at or above the levels expressed in *Atxn1(175Q)* mice.

Figure 4H depicts the relationship between the extractability of ATXN1[175Q]K772T and the proportion of ATXN1[175Q]K772T found in the cytoplasm for the different brain regions assessed. With the exception of the medulla, there was a strong positive correlation between extractability and cytoplasmic proportion of ATXN1[175Q]K772T. The extractability results seen in the medulla of *Atxn1(175Q)K772T* mice were a clear outlier

Author Manuscript Author Manuscript Author Manuscript Author Manuscript

compared to the other brain regions as ATXN1[175Q]K772T was more extractable than the WT protein product, ATXN1[2Q], in this region.

Once in the nucleus, expanded ATXN1 accumulates into punctate inclusions.[27] To assess the effect of the NLS mutation on nuclear localization of ATXN1[175Q] at a cellular level, we quantified ATXN1 nuclear inclusions in brain regions associated with SCA1-like phenotypes. Perfused brain tissue from *Atxn1(175Q)* and *Atxn1(175Q)K772T* mice was immunofluorescently labeled for ATXN1 and NUP62, a nuclear membrane marker (Figure 5). An Imaris pipeline was developed to generate a nuclear mask using the NUP62 staining, remove all fluorescent ATXN1 signal outside of the nuclear mask (Figure 5B, 5E), and analyze only ATXN1 staining within the cellular nucleus (under the mask) (Figure 5C, 5F). In each brain region, the percentage of all cells analyzed with at least one nuclear inclusion was recorded for each mouse. Since cerebellar Purkinje cells do not develop nuclear inclusions until relatively late in disease progression,[14] this cell population was analyzed in *Atxn1(175Q)* and *Atxn1(175Q)K772T* mice at 21 weeks of age. No Purkinje cell inclusions were observed at this age for the *Atxn1(175Q)K772T* mice while over half of the *Atxn1(175Q)* Purkinje cells had at least 1 inclusion, which amounted to a significant difference ($p<0.0001$) in inclusion frequency between the two genotypes (Figure 5G). Nuclear inclusions were assessed in ventral medulla (Figure 6H and Figure S6), cerebral cortex (Figure 6I), CA1 of the hippocampus (Figure 6J), and dorsal striatum (Figure 6K) at 12 weeks of age because inclusions are typically present in *Atxn1*$^{154Q/2Q}$ mice by this time point in these regions. At this age, the medulla was the only brain region with a significant difference ($p=0.0456$) in number of cells with a nuclear inclusion between *Atxn1(175Q)* and *Atxn1(175Q)K772T* mice. There were no inclusions detected in any of the medulla cells in *Atxn1(175Q)K772T* mice and there was a large range in the number of medulla cells with an inclusion across the 175Q mice assessed. To determine whether the NLS mutation impacted the formation of nuclear inclusions in cerebral cortex, dorsal striatum, and CA1 of the hippocampus earlier in disease progression, these regions were assessed at 5 weeks of age (Figure 6L-N and Figure S6). At this age, there was a significant difference in in number of cells with a nuclear inclusion between *Atxn1(175Q)* and *Atxn1(175Q)K772T* mice for all three brain regions assessed. These findings indicate that the nuclear inclusion formation process is markedly delayed in mice with the NLS mutation. Additionally, the results show that the timing of nuclear inclusion formation is brain-region specific.

To further characterize the cellular pathology and distribution of nuclear inclusions throughout the brain, we assessed the extent to which ATXN1 inclusions were ubiquitinated. In 12-week-old *Atxn1(175Q)* and *Atxn1(175Q)K772T* mice, nuclear inclusions were assessed in CA1 of the hippocampus (Figure S6A), cerebral cortex (Figure S6B), and dorsal striatum (Figure S6C). In the ventral medulla, the ubiquitin status of ATXN1 inclusions was determined at 12 weeks (Figure S6D) and 25 weeks of age (Figure S6E). At 12 weeks of age, for all brain regions assessed, ubiquitinated ATXN1 inclusions were detected in *Atxn1(175Q)* mice (Figure S6). In dorsal striatum at 12 weeks of age, ubiquitinated ATXN1 inclusions were greatly reduced in *Atxn1(175Q)K772T* mice compared to *Atxn1(175Q)* mice (Figure S6C). In ventral medulla, ubiquitinated ATXN1 inclusions were only seen in 12-week-old *Atxn1(175Q)* mice (Figure S6D). In contrast, by 25 weeks of age, ubiquitinated ATXN1 inclusions were prevalent in the ventral medulla of *Atxn1(175Q)* mice and greatly

Author Manuscript Author Manuscript Author Manuscript Author Manuscript

reduced in *Atxn1(175Q)K772T* mice (Figure S6E). In *Atxn1(175Q)* mice, ubiquitinated ATXN1 inclusions were detected throughout the cerebellum with Purkinje cells typically having one very prominent nuclear inclusion (Figure S7A). As seen in Purkinje cell-specific ATXN1[82Q] transgenic mice,[2] the K772T NLS mutation eliminated Purkinje cell ubiquitinated ATXN1 inclusions in 25-week-old *Atxn1(175Q)K772T* mice (Figure S7B). Notably, ubiquitinated ATXN1 inclusions were present in other cerebellar cells of *Atxn1(175Q)K772T* mice. These findings indicate that, while nuclear inclusion formation/ubiquitination throughout the brain is reduced in mice with the NLS mutation, the extent to which nuclear inclusion formation/ubiquitination is decreased in *Atxn1(175Q)K772T* mice varies considerably between brain regions and cell types.

Mutation of the ATXN1[175Q] NLS restores disease-associated transcriptomic expression profiles of brain regions in a regionally unique manner

To evaluate the effect of the NLS mutation on gene expression, RNAseq was performed on lysates from cerebellum, medulla, cortex, striatum, and hippocampus tissue in WT, *Atxn1(175Q),* and *Atxn1(175Q)K772T* mice at 26 weeks of age. The number of significantly differentially expressed genes (DEGs) in the pairwise comparison between WT and *Atxn1(175Q)* mice was much larger than the number of DEGs in the pairwise comparison between WT and *Atxn1(175Q)K772T* for all brain regions assessed (Figure 6A). Although the cortex, striatum, and hippocampus had the largest total number of DEGs for both genotype comparisons, the cerebellum and medulla had the largest proportion of genes corrected by the NLS mutation. A gene was considered to be corrected by the NLS mutation if it was significantly differentially expressed between WT and *Atxn1(175Q)* mice and not significantly differentially expressed between WT and *Atxn1(175Q)K772T* mice. These results show that the NLS mutation has a substantial influence on transcriptomic profile throughout the brain, but its strongest impact was on the cerebellum and medulla.

To further study the groups of corrected genes, several analyses focused on the top 500 corrected genes in each brain region, defined as corrected genes with the largest absolute value Log_2(Fold Change) in the comparison between WT and *Atxn1(175Q)* mice. The software used for pathway analysis is optimized to analyze 250-1250 genes per brain region. Within that range, we aimed to compare the same number of genes from each brain region and to maximize the number of genes analyzed from each brain region while ensuring that no region had all corrected genes included. Since the cerebellum had the smallest absolute number of corrected genes (n=624), 500 genes per brain region was chosen to capture as much information from the dataset as possible. UpSetR[28] was used to generate a diagram showing the number of top corrected genes from each brain region that were found to be unique to a particular region or shared by any combination of brain regions (Figure 6B). For all five brain regions assessed, the majority (>60%) of the top 500 corrected genes were unique to that brain region.

To date, three transcription factors are known to interact with ATXN1: Capicua (CIC),[29] Regulatory factor 1 (RFX1), and Zinc finger with KRAB and SCAN domains 1 (ZKSCAN1).[30] Enrichment of the consensus CIC, RFX1, and ZKSCAN1 binding motifs among the promoter regions of the complete set of corrected genes from each brain region

Author Manuscript Author Manuscript Author Manuscript Author Manuscript

was examined relative to genes that are not significantly differentially expressed at 10 weeks of age. Binding motifs for all three transcription factors were enriched among the corrected genes in all brain regions except for ZKSCAN in the cerebellum (Figure 6C-E). This suggests that these transcription factors play a critical role in regulating the expression of genes corrected by the NLS mutation.

The top 500 corrected genes from each brain region were assessed for pathway enrichment using clusterProfiler[31] (Figure 7). In looking for enrichment of pathways in the molecular function domain of the Gene Ontology database, the cerebellum stands out as having unique pathway enrichment with no overlap among the other brain regions assessed. Interestingly, the two regions showing the most prominent pathology in SCA1 patients, the cerebellum and medulla, have no overlaping corrected pathways. These results provide further support for the idea that pathological mechanisms downstream of nuclear entry of expanded ATXN1 have regional specificity.[32]

DISCUSSION

While neurodegenerative diseases are often associated with prominent pathology in a certain brain region or neuronal population, many disorders impact diverse structures, circuitry, and cell populations that lack obvious pathology. In the case of SCA1, cerebellar Purkinje cell degeneration is a frequent and prominent pathological feature. Yet, SCA1 patients present with symptoms linked to multiple different brain regions.[12,13] Previously, we showed that nuclear localization of expanded ATXN1 is critical for pathogenesis in cerebellar Purkinje cells.[2] In this study, we assessed the importance of ATXN1 nuclear localization beyond the cerebellum and characterized its role in molecular aspects of disease in diverse brain regions associated with SCA1-like phenotypes. We found that mutating the NLS of expanded ATXN1[175Q] in a knock-in mouse model of SCA1 reduced nuclear localization of the expanded protein and dramatically mitigated a spectrum of phenotypes characteristic of SCA1.

Severity of SCA1-like phenotypes are reduced in *Atxn1(175Q)K772T* mice

Complete rescue of rotarod performance was observed when the NLS mutation was introduced into ATXN1[82Q] expressed exclusively in Purkinje cells of a transgenic SCA1 mouse model.[2] In contrast, while the rotarod performance of *Atxn1(175Q)K772T* mice was significantly improved compared to *Atxn1(175Q)* mice, there was not a complete rescue as *Atxn1(175Q)K772T* mice did not perform as well as WT mice at any age assessed. Notably, at 6 weeks of age, improvement of performance across successive trial days (i.e. motor learning) in naïve mice, was not restored in *Atxn1(175Q)K772T* mice (Figure 2A). This finding suggests that the inability to learn on the rotarod by *Atxn1(175Q)* mice is not solely due to Purkinje cell dysfunction induced by nuclear localization of ATXN1[175Q] (see below). Contrary to the motor learning findings, the severe decline in motor performance with increasing age observed in *Atxn1(175Q)* mice was rescued in *Atxn1(175Q)K772T* mice (Figure 2B), indicating that nuclear localization of ATXN1[175Q] influences motor function over time. Whether this age-dependent loss in motor performance is due to nuclear localization of ATXN1[175Q] exclusively in Purkinje cells remains to be determined.

Author Manuscript Author Manuscript Author Manuscript Author Manuscript

Mutation of the ATXN1[175Q] NLS nearly doubled the lifespan of *Atxn1(175Q)K772T* mice relative to *Atxn1(175Q)* mice (Figure 2C). This extension is among the most substantial survival study results seen in animal models of SCA1.[30,32,33] Thus, proper nuclear localization plays a critical role in the pathological dysfunction that underlies the premature lethality of *Atxn1(175Q)* mice. Similar to SCA1 patients, lethality in knock-in SCA1 mouse models is thought to result from complications due to bulbar, medulla, and brainstem dysfunction leading to breathing problems.[6,7,9] Accordingly, developing an understanding of why cells involved in premature lethality mechanisms are particularly responsive to the NLS mutation is a critical next step and has strong potential for therapeutic application.

Across the other phenotypes assessed, *Atxn1(175Q)K772T* mice consistently performed significantly better than *Atxn1(175Q)* mice, but not as well as WT mice. This suggests that nuclear localization plays a critical role in a variety of different brain regions and wide range of disease-related metrics, but the NLS mutation alone does not completely halt pathogenesis. Subcellular fractionation results indicate that the NLS mutation significantly hindered but did not completely inhibit expanded ATXN1 from entering the nucleus (Figure 4). It is currently unclear whether the observed partial restoration of SCA1 phenotypes in Atxn1(175Q)K772T mice is due to the remaining expanded ATXN1 present in the nucleus or aspects of pathogenesis occurring outside of the nucleus.

Striatal pathology in *Atxn1(175Q)* mice

Figure 2A and 2B show that the NLS mutation in the *Atxn1(175Q)K772T* mice mitigates the decline in motor performance and coordination observed with aging in *Atxn1(175Q)* mice. However, naïve *Atxn1(175Q)K772T* mice, like *Atxn1(175Q)* mice, were unable to learn with training. In contrast, in transgenic mice where mutant ATXN1 expression is restricted to cerebellar Purkinje cells, the K772T mutation restores all aspects of rotarod performance, including learning.[2] Thus, we suggest that failure to learn on the rotarod is due to pathogenic effects of ATXN1[175Q] in cells or regions other than Purkinje cells. The striking striatal decrease of DARPP-32 expression along with reduced expression of D1 and D2 receptor mRNA (Figure 3) from both *Atxn1(175Q)* and *Atxn1(175Q)K772T* mice provides support for a pathogenic effect of ATXN1[175Q] in the striatum of these mice. Given that the striatum is a region known to have a critical role in motor learning,[19] we speculate that the rotarod learning difficulties observed for *Atxn1(175Q)* and *Atxn1(175Q)K772T* mice may be the result of changes in striatal gene expression that are not corrected by the NLS alteration, e.g. striatal DARPP-32, *Drd1,* and *Drd2* levels are similarly reduced for both *Atxn1(175Q)K772T and Atxn1(175Q)* mice (Figure 3). Thus, we suggest that, unlike cerebellar Purkinje cells and cells of the medulla, where nuclear entry of mutant ATXN1 is critical for pathogenesis, the striatal pathogenic effect of mutant ATXN1 is likely due to actions outside of the cellular nucleus.

ATXN1 extractability, subcellular localization, and nuclear inclusion formation in *Atxn1(175Q)K772T* mice

As noted previously, the extractability of expanded ATXN1 declined with age throughout the brain of *Atxn1(175Q)* mice (Figure S3 and Figure S4). The extractability of

Author Manuscript Author Manuscript Author Manuscript Author Manuscript

ATXN1[175Q]K772T also declined with age but was significantly greater than the extractability of ATXN1[175Q] in all brain regions at all ages, suggesting that extractability of expanded ATXN1 decreases upon localization to the nucleus. Consistent with this concept is the strong correlation between the extraction of ATXN1[175Q]K772T at 40 weeks of age and its cytoplasmic proportion at 26 weeks-of-age for all brain regions examined except the medulla (Figure 4H).

In the medulla, ATXN1[175Q]K772T extractability relative to its cytoplasmic proportion was much greater than in the other brain regions and was even greater than ATXN1[2Q]. Previously, it was shown that ATXN1 with an expanded polyQ tract is more resistant to degradation than WT ATXN1.[34] We suggest that in the medulla, where solubility of mutant ATXN1 is higher than in other brain regions, the enhanced amounts of ATXN1[175Q]K772T relative to WT ATXN1 reflects increased stability of the expanded protein relative to ATXN1[2Q]. Regardless, analysis of the subcellular distribution of ATXN1[175Q]K772T indicates that the nuclear proportion in the medulla was very similar to the proportion of nuclear ATXN1[175Q]K772T in the other regions of the brain (Figure 4 and Figure S2). Moreover, at both 5 and 26 weeks of age, ATXN1[175Q] was more extractable from the medulla than the other regions of the brain (Figure S3D-F and 4H). Once in the nuclei of cells in the medulla, expanded ATXN1 remains more soluble than it does in the nuclei of cells in other brain regions. This finding further supports the concept that mutant ATXN1 pathogenesis is not dependent on the formation of insoluble inclusions/complexes.[2,14,34]

Consistent with the subcellular fractionation data, the presence of ATXN1 nuclear inclusions with age in *Atxn1(175Q)K772T* mice supports the conclusion that entry of mutant protein into the nucleus is not completely blocked by the NLS mutation. Although some expanded ATXN1 enters the nucleus in *Atxn1(175Q)K772T* mice, the age at which nuclear inclusions form is delayed relative to *Atxn1(175Q)* mice across all brain regions assessed (Figure 5, S6D, and S6E). There is no detectable change in the nuclear proportion of ATXN1 in the cortex, hippocampus, medulla, or striatum of *Atxn1(175Q)K772T* mice between 5 and 40-42 weeks of age (Figure 4), but there is an increase in the proportion of cells with nuclear inclusions in these regions with age (Figure 5). Thus, we suggest that nuclear inclusions are a sensitive marker of levels of expanded ATXN1 in the nucleus. The contribution of ATXN1 nuclear inclusions to the reduction in extractability of expanded ATXN1 remains unclear. Regardless, we believe that the findings reported here support that, similar to mutant ATXN1-induced Purkinje cell pathogenesis,[2,14,34] pathogenesis throughout the brain is not dependent on the formation of insoluble inclusions/complexes. For example, mutant ATXN1 solubility is very high in the medulla, yet the medulla is a major site of SCA1 pathogenesis. Further, in the cortex, hippocampus, and striatum of *Atxn1(175Q)K772T* mice, inclusion numbers are not significantly different from those observed in *Atxn1(175Q)* mice at 12 weeks of age (Figure 5). Yet, with increasing age, *Atxn1(175Q)K772T* mice show mitigated SCA1-like phenotypes (Figure 2) and fewer genetic expression perturbations (Figure 6A) relative to *Atxn1(175Q)* mice.

Author Manuscript Author Manuscript Author Manuscript Author Manuscript

Distinct brain region molecular disease-associated signatures

Previous RNAseq studies indicate that molecular aspects of pathogenesis, as assessed by characterization of DEGs, differed between the cerebellum and medulla[32] and between the cerebellum and inferior olive.[35] A recent study found that *Atxn1*$^{154Q/2Q}$ knock-in mice had both shared and region-specific transcriptomic changes in the cerebellum and cerebral cortex.[36] Here, we utilized RNAseq to identify DEGs with expression corrected by the NLS mutation in the cerebellum, medulla, hippocampus, cerebral cortex, and striatum. The NLS mutation substantially reduced the number of DEGs throughout the brain of *Atxn1(175Q)K772T* mice (Figure 6A).

The largest proportional impact of the NLS mutation on correcting DEGs was in the cerebellum (87% corrected) and medulla (90% corrected), which paralleled the strong age-related improvement of motor performance and extended survival associated with the NLS mutation. Moreover, the concept that disease-associated DEGs differ among brain regions is supported by analyses of the top 500 genes corrected by the NLS mutation from each brain region. First, the vast majority of the top 500 corrected genes are unique to each brain region (Figure 6B). Additionally, pathway enrichment analysis of the top 500 corrected genes from each brain revealed that while there is some overlap in pathway enrichment between brain regions, particularly between the cortex and hippocampus, most regions show a unique pathway enrichment profile (Figure 7). Notably, the cerebellum displays unique enrichment of genes associated with channel activity and cellular signaling. The pathways enriched among corrected genes in the cerebellum overlap substantially with pathways previously recognized as dysfunctional in Purkinje cell disease pathology and found to be corrected by administration of an *Atxn1*-targeting antisense oligonucleotide.[32,37] Additionally, this finding is consistent with work showing that early changes in expression of specific ion-channels and receptors are important for regulating membrane excitability and contribute to both motor dysfunction and structural changes in neurons that consistently precede cell death.[1,38]

Among the top corrected genes in the cerebral cortex were those encoding proteins involved in the regulation of protein phosphorylation (Figure 7). This is consistent with a recent study showing that the disease-associated DEG signature of the cortex in *Atxn1*$^{154Q/2Q}$ knock-in mice is enriched for genes related to phosphorylation and kinase regulation.[36] The top corrected genes in the medulla are uniquely enriched for pathways related to neurotransmitter trafficking and postsynaptic activity. It is possible that dysfunction in vesicle transportation and postsynaptic response to neurotransmitter release drives breathing difficulties and premature lethality in SCA1. Thus, correction of these pathways towards WT functionality may explain the observed extension in lifespan among *Atxn1(175Q)K772T* mice (Figure 2C). Overall, these results indicate that diseased-associated transcriptomic profiles are largely unique to each brain region assessed.

In summary, this study demonstrates that proper nuclear localization of expanded ATXN1 is an important aspect of pathogenesis across the spectrum of phenotypes characteristic of SCA1. Thus, it will be important to perform additional studies to better understand the regulation of ATXN1 nuclear localization in the different regions of the brain affected in SCA. Further, it will be prudent to characterize striatal pathogenic pathways that could

Author Manuscript Author Manuscript Author Manuscript Author Manuscript

potentially be independent of mutant ATXN1 nuclear localization. Regardless, we argue that the results of this study indicate that inhibition of ATXN1 nuclear entry has considerable potential as a therapeutic approach for SCA1.

STAR METHODS

RESOURCE AVAILABILITY

Lead Contact—Further information and requests for resources and reagents should be directed to the lead contact, Harry T. Orr (orrxx002@umn.edu).

Materials Availability

Data and Code Availability: All RNA sequencing FASTQ data files have been deposited to SRA accession #PRJNA903137. RNA sequencing counts data and differential expression data have been deposited to GEO accession GSE218303. Accession numbers are listed in the key resources table. This paper does not report original code. Any additional information required to reanalyze the data reported in this paper is available from the lead contact upon request.

EXPERIMENTAL MODEL AND SUBJECT DETAILS

Mice—The University of Minnesota Institutional Animal Care and Use Committee approved all animal use protocols. All mice were housed and managed by Research Animal Resources under specific pathogen-free conditions in an Association for Assessment and Accreditation of Laboratory Animal Care International approved facility. The mice had unrestricted access to food and water except during behavioral testing. In all experiments, equal numbers of male and female mice were used. All mice were age matched within experiments and littermate controls were used when possible.

All mice were maintained on a C57BL/6 genetic background. WT ($Atxn1^{2Q/2Q}$) mice were ordered from The Jackson Laboratory. $Atxn1^{175Q/2Q}$ mice are the result of spontaneous trinucleotide repeat expansion in the *Atxn1* gene of $Atxn1^{154Q/2Q}$ mice that were previously described.[14]

Generation of $Atxn1^{175QK772T/2Q}$ mouse model—$Atxn1^{175QK772T/2Q}$ mice were generated via CRISPR-Cas9-mediated gene editing.[39,40] The guide RNA sequence (5'-CGACCACCTCCTCTTCCTCG-3') was selected based on the highest on-target potential and the lowest off target risk using the Custom Alt-R CRISPR-Cas9 guide RNA design software (Integrated DNA Technologies). Based on guidance from the University of Minnesota Genome Engineering Shared Resource, this guide RNA (sgRNA) with a modified EZ scaffold was purchased from Synthego.

A single-stranded oligonucleotide (ssODN) was purchased from Integrated DNA Technologies as a template for homologous-directed recombination to introduce the K772T alteration and another synonymous mutation to endogenous *Atxn1* (5'-AAAATAGGATTGCCTGCAGCACCCTTCCTCAGCAAAATAGAACCGAGCAAACCCACAGCtACGAGGAccAGGAGGTGGTCGGCGCCGGAGACCCGTAAACTGGAGAAGTC

Author Manuscript Author Manuscript Author Manuscript Author Manuscript

GGAGGACGAGCCACCTTTGA-3'; modified nucleotides are lowercase). Two nucleotide modifications were required to introduce the K772T alteration. The other nucleotide alteration serves two functions: ablation of the PAM site and introduction of an Alu1 enzyme digest site used for genotyping.

Prior to injecting mouse embryos, accurate targeting of the sgRNA and introduction of the desired nucleotide alterations via homologous-directed recombination by the ssODN was confirmed by the University of Minnesota Genome Engineering Shared Resource in NIH3T3 cells.

At the University of Minnesota Mouse Genetics Laboratory (MGL), female C57BL/6 mice were super-ovulated via injection of pregnant mares serum gonadotropin followed by injection of human chorionic gonadotropin 48 hours later. The females were then bred to *Atxn1*$^{175Q/2Q}$ males overnight and zygotes were collected the following day. An injection mixture containing 39.6ng/μL Cas9 protein (Integrated DNA Technologies), 7ng/μL sgRNA, and 20ng/μL ssODN was prepared per MGL protocols and injected into the pronucleus of extracted zygotes. Zygotes were then transferred by MGL into oviducts of pseudopregnant females. Offspring resulting from this procedure were genotyped using the protocols in the following section. Integration of desired nucleotide changes on the expanded *Atxn1* allele was confirmed by Sanger sequencing. The mice were backcrossed for a minimum of 3 generations before conducting molecular or behavioral assays to avoid off-target effects.

Genotyping—PCR was performed with the following primers (Integrated DNA Technologies) to determine which animals have an expanded *Atxn1* allele: *Atxn1* 175Q Forward (5'-ACCTTCCAGTTCATTGGGTC-3') and *Atxn1* 175Q Reverse (5'-GCTCTGTGGAGAGCTGGA-3'). To assess the presence of the K772T alteration, PCR was performed using the following primers: K772T Forward (5'-GCCGTGTTCCAAACTCTCTG-3') and K772T Reverse (5'-GGTCTCTACTTGCCCACGTTA-3') (Integrated DNA Technologies) followed by an Alu1 restriction enzyme digest (New England BioLabs).

METHOD DETAILS

Behavioral Analyses—Investigators were blinded to the genotype of the mice for all behavioral analyses. *Atxn1*$^{2Q/2Q}$, *Atxn1*$^{175Q/2Q}$, and *Atxn1*$^{175QK772T/2Q}$ mice were used in all behavioral tests. Mice were habituated to the testing room for at least 15 min prior to the start of testing on each day. All testing apparatus was cleaned between each animal with 70% ethanol.

Rotarod: The same cohort of mice was tested at 6, 12, 18, and 24 weeks of age. Mice were assessed on rotarod apparatus (Ugo Basile) using an accelerating protocol: 5 to 50 rpm, 5-min ramp duration, 5-min maximum trial length. The test consisted of a total of 4 trials per day for 4 consecutive days. Animals were segregated by sex during testing and run in consistent groups (up to 5 at a time). To ensure enough recovery time between trials, animals were given 10-15 min to rest between successive trials, which included the time used to test the other groups in the trial. A trial ended when an animal failed to stay on the rotarod or if they made 2 consecutive rotations clinging to the rod and not ambulating.

Author Manuscript Author Manuscript Author Manuscript Author Manuscript

Barnes Maze: The same cohort of mice was assessed at 7 and 17 weeks of age. The maze is a circular table 92cm above the floor with a diameter of 92cm. The table has twenty circular holes located at equal distances around the perimeter, each with a diameter of 5 cm. One hole (the target hole) leads to a 5.7cm wide × 11.5cm long × 6.4cm deep escape chamber in which the animal can hide, and the other 19 holes were closed. Illumination at the center of the table is maintained at 250 lux until the mouse enters the escape chamber to motivate them to search for the target hole. The testing room had visual cues on the walls to serve as landmarks. The position of each mouse was tracked using ANY-maze (Stoelting). Mice were exposed to the maze for 4 3-min trials per day (intertrial interval of approximately 10 min) during 4 consecutive training days. Mice that did not enter the escape box within 3 min were gently guided to it. To eliminate odor tracking and ensure mice only used spatial cues, the maze was rotated 90° between each trial while maintaining the location of the escape box in relation to the rest of the room. Video footage of mice traveling to the escape chamber during training was analyzed using the Barnes-maze unbiased strategy (BUNS) algorithm[26] to classify search strategies and score cognitive performance.

Contextual Fear Conditioning: Mice were assessed at 8 weeks of age. They were trained in a fear-conditioning chamber (Med Associates) that can deliver an electric shock paired with a tone. This device was located inside a soundproof box that contained a digital camera. Each mouse was placed individually in the chamber for habituation and left undisturbed for 3 min. Each mouse was given 5 fear acquisition stimuli foot-shocks (2s, 0.7mA) at varying intervals over a 7 min period (the shock timing pattern was consistent across all mice tested). The mouse was then returned to its home cage overnight. Contextual fear memory was assessed 24 hours after training. Mice were placed in the fear acquisition environment for 3 min without a foot-shock. For all training sessions and trials, mouse movement was recorded and analyzed using Video Freeze software (Med Associates). Freezing was scored only if the animal was immobile for at least 500ms.

Western Blots

Subcellular Fractionation: Cerebellum, medulla, cerebral cortex, hippocampus, and striatum tissue was collected from *Atxn1*$^{175QK772T/2Q}$ and *Atxn1*$^{175Q/2Q}$ mice at 5 weeks of age and from *Atxn1*$^{175QK772T/2Q}$ mice at 40-42 weeks of age. Cytoplasmic and nuclear protein extracts were collected using the NE-PER kit (Thermo Fisher Scientific). Protein concentrations were measured using the Pierce BCA Protein Assay kit (Thermo Fisher Scientific). Cytoplasmic and nuclear samples from each brain region containing 5μg total protein were boiled in Laemmli loading buffer and run on a 4%–20% Bio-Rad precast gel. Protein was transferred to a nitrocellulose membrane using the BioRad Trans-Blot Turbo system. Blots were cut at approximately 75kDa and blocked overnight at 4°C in 5% milk PBST (phosphate-buffered saline, 0.1% Tween 20). Blot sections were probed overnight at 4°C 1:5000 with the ATXN1 antibody 11750[41] or 1:2500 with H1 antibody (Invitrogen) diluted in 5% milk PBST. Blots were washed 3 times with PBST and then placed in 5% milk PBST plus 1:2500 rabbit specific horseradish peroxidase (HRP) antibodies (GE Healthcare) at room temperature for 4 hours. Blots were washed 3 times with PBST followed by Super Signal West Dura (Thermo Fisher Scientific) detection reagents and imaged on an

Author Manuscript Author Manuscript Author Manuscript Author Manuscript

ImageQuant LAS 4000. The H1 blots were stripped with Restore Western Blot Stripping Buffer (Thermo Fisher Scientific) for 15 min at room temperature, washed 3 times with PBST, and blocked overnight at 4°C in 5% milk PBST. These blots were then probed overnight at 4°C 1:1000 with GAPDH antibody (EMD Millipore Corp), washed 3 times with PBST, placed in 5% milk PBST plus 1:2500 mouse specific HRP antibodies (GE Healthcare) at room temperature for 4 hours, and visualized via the same method as the ATXN1 and H1 blots.

ATXN1 Extraction: Cerebellum, medulla, cerebral cortex, hippocampus, and striatum tissue was collected from *Atxn1*$^{2Q/2Q}$, *Atxn1*$^{175QK772T/2Q}$ and *Atxn1*$^{175Q/2Q}$ mice at 5 weeks and 26 weeks of age. Samples were homogenized using a tissue grinder in an appropriate volume (350µl for medulla and striatum, 500µl for cerebellum, cortex, and hippocampus) of Tris Triton lysis buffer (50mM Tris, pH 7.5, 100mM NaCl, 2.5mM MgCl2, 0.5% Triton X-100) that included MilliporeSigma protease inhibitors II and III and a Roche Complete Mini Protease inhibitor tablet. Homogenized samples were shaken at 1500rpm at 4°C for 1 hour, frozen and thawed in liquid nitrogen and 37°C water bath 3 times, and centrifuged at 21,000xg for 10 min at 4°C. Samples containing 30µg total protein were boiled in Laemmli loading buffer and run on a 4%–20% Bio-Rad precast gel. Protein was transferred to a nitrocellulose membrane using the BioRad Trans-Blot Turbo system. Blots were cut at approximately 75kDa and blocked overnight at 4°C in 5% milk PBST (phosphate-buffered saline, 0.1% Tween 20). Blots were probed overnight at 4°C 1:5000 with the ATXN1 antibody 11750[41] or 1:10,000 with α-Tubulin antibody (MilliporeSigma) diluted in 5% milk PBST. Blots were washed 3 times with PBST. ATXN1 blots were then placed in 5% milk PBST plus 1:2500 rabbit specific HRP antibodies (GE Healthcare) while α-Tubulin blots were placed in 5% milk PBST plus 1:10,000 mouse specific HRP antibodies (GE Healthcare) at room temperature for 4 hours. Blots were washed 3 times with PBST and then ATXN1 blots were washed with Super Signal West Dura (Thermo Fisher Scientific) while α-Tubulin blots were washed with Super Signal West Pico (Thermo Fisher Scientific) detection reagents. Blots were imaged on an ImageQuant LAS 4000.

DARPP-32 Quantification: Striatum tissue was collected from *Atxn1*$^{2Q/2Q}$, *Atxn1*$^{175QK772T/2Q}$ and *Atxn1*$^{175Q/2Q}$ mice at 10 weeks of age. Samples were homogenized using a tissue grinder in 350µl Tris Triton lysis buffer (50mM Tris, pH 7.5, 100mM NaCl, 2.5mM MgCl2, 0.5% Triton X-100) that included MilliporeSigma protease inhibitors II and III and a Roche Complete Mini Protease inhibitor tablet. Homogenized samples were shaken at 1500rpm at 4°C for 1 hour, frozen and thawed in liquid nitrogen and 37°C water bath 3 times, and centrifuged at 21,000xg for 10 min at 4°C. Samples containing 30µg total protein were boiled in Laemmli loading buffer and run on a 4%–20% Bio-Rad precast gel. Protein was transferred to a nitrocellulose membrane using the BioRad Trans-Blot Turbo system. Blots were cut at approximately 75kDa and blocked overnight at 4°C in 5% milk PBST (phosphate-buffered saline, 0.1% Tween 20). Blot was probed overnight at 4°C 1:1000 with DARPP-32 antibody (R&D Systems) or 1:5000 with α-Tubulin antibody (MilliporeSigma) diluted in 5% milk PBST. Blots were washed 3 times with PBST. DARPP-32 blots were then placed in 5% milk PBST plus 1:2500 rat specific HRP antibodies (GE Healthcare) while α-Tubulin blots were placed in 5% milk PBST plus 1:10,000 mouse specific HRP

Author Manuscript Author Manuscript Author Manuscript Author Manuscript

antibodies (GE Healthcare) at room temperature for 4 hours. Blots were washed 3 times with PBST and then DARPP-32 blots were washed with Super Signal West Dura (Thermo Fisher Scientific) while α-Tubulin blots were washed with Super Signal West Pico (Thermo Fisher Scientific) detection reagents. Blots were imaged on an ImageQuant LAS 4000.

Immunofluorescence

ATXN1 inclusions: Mice were deeply anesthetized with Ketamine, transcardially exsanguinated with PBS, and perfused using 10% formalin. Brains were post-fixed overnight in 10% formalin then stored in PBS at 4°C until sectioning. Sagittal sections of 50μm were isolated using a Leica VT 1000S vibratome. Sections were permeabilized in 1% Triton X-100 in PBS. Sections were blocked for 1 hour in 5% normal donkey serum and 0.3% Triton X-100 in PBS. Subsequent staining was carried out in 2% normal donkey serum and 0.3% Triton X-100 in PBS. Sections were incubated for 48 hours with primary antibodies 1:1000 anti-mouse NUP62 (BD Biosciences), 1:500 anti-rabbit ATXN1 (12NQ)[42], and 1:500 anti-guinea pig CALB1 (Synaptic Systems)) at 4°C. Following incubation, sections were washed four times in PBS and exposed to secondary antibodies (Jackson Immunoresearch Labs Alexa Fluor 488 anti-mouse, Cy3 anti-rabbit, and Alexa Fluor 647 anti-guinea pig) for 24 hours at 4°C. Sections were washed four times in PBS and mounted using ProLong Gold antifade reagent (Thermo Fisher Scientific). Fluorescently labeled tissue was imaged with 488/559/635nm lasers using an Olympus Fluoview 1000 IX2 inverted confocal microscope with a 40x oil immersion objective (NA 1.3) with an xy voxel size of 0.305-0.450μm and z-step size of 0.84μm. Fluorescent emissions were detected using photomultiplier tubes with spectral ranges of 500-545nm (Alexa Fluor 488), 575-620nm (Cy3), and 655-755nm (Alexa Fluro 647) with the confocal aperture set to 85μm. Images from each brain region were captured using identical acquisition settings for $Atxn1^{175QK772T/2Q}$ and $Atxn1^{175Q/2Q}$ samples. Nuclear ATXN1 inclusions were analyzed using batched processes developed with Imaris (Oxford Instruments, v9.8). The Imaris surfaces module was used to isolate nuclear ATXN1 staining by creating a nuclear mask from NUP62 staining and to identify nuclear ATXN1 inclusions. Inclusion identification used identical thresholding parameters for $Atxn1^{175QK772T/2Q}$ and $Atxn1^{175Q/2Q}$ samples and was adjusted between tissue regions to reduce background detection. Inclusion identification was batched for all images from the same tissue region and background was further eliminated using a $1um^3$ volume filter. Incomplete or “chopped” inclusions were removed with a z-filter. Complete inclusions were analyzed by volume and mean fluorescent intensity of the filtered inclusion surfaces. Inclusion frequency was determined by using the Imaris spots module to count nuclear ATXN1 inclusions and NUP62-labled nuclei.

Ubiquitination staining: 50μm sagittal sections were cut using a Leica VT 1000S vibratome. Epitope retrieval was performed in 10 mM Sodium Citrate 0.05% Tween-20 at 95°C for 15 minutes, and then permeabilized in 1% Triton X-100 in PBS 15 minutes before blocking in 5% normal goat serum. Sections were incubated for 48 hours with primary antibodies 1:500 anti-mouse ubiquitin (ThermoFisher), 1:500 anti-rabbit ATXN1 (12NQ),[42]and 1:500 anti-guinea pig CALB1 (Synaptic Systems)) at 4°C. Following incubation, sections were washed four times in PBS and exposed to secondary antibodies (Jackson Immunoresearch Labs Alexa Fluor 488 anti-mouse, Cy3 anti-rabbit, and Alexa

Author Manuscript Author Manuscript Author Manuscript Author Manuscript

Fluor 647 anti-guinea pig) for 24 hours at 4°C. Sections were washed four times in PBS and mounted using ProLong Gold antifade reagent (Thermo Fisher Scientific). Confocal 1.0 micron z-stacks were collected on the Olympus Fluoview 1000 IX2 inverted confocal microscope with a 60x oil immersion objective. Images were merged using Fiji (v2.0.0).

RNA Extraction and Sequencing—Cerebellum, cerebral cortex, hippocampus, and striatum tissue was isolated from 10-week-old and 26-week-old *Atxn1*$^{2Q/2Q}$, *Atxn1*$^{175QK772T/2Q}$, and *Atxn1*$^{175Q/2Q}$ mice and stored in RNA*later* solution (Thermo Fisher Scientific). Additionally, whole-brainstem samples were included at 10 weeks of age and medulla samples were included at 26 weeks of age. Total RNA was isolated using TRIzol reagent (Thermo Fisher Scientific) following the manufacturer's protocols. Tissue was homogenized using RNase-Free disposable pellet pestles in a motorized chuck. Purified RNA was sent to the University of Minnesota Genomics Center for quality control, including quantification using fluorimetry via RiboGreen assay kit (Thermo Fisher Scientific) and RNA integrity was assessed via capillary electrophoresis using an Agilent BioAnalyzer 2100 to generate an RNA integrity number (RIN). RIN values for submitted RNA were above 8.0 for all samples except one medulla sample (RIN = 6.8). All submitted RNA samples had greater than 1μg total mass except one 10-week-old Atxn12Q/2Q striatum sample (0.655 μg). Library creation was completed using oligo-dT purification of polyadenylated RNA, which was reverse transcribed to create cDNA. cDNA was fragmented, blunt ended, and ligated to barcode adaptors. Libraries were size selected to 320 bp ± 5% to produce average inserts of approximately 200 bp, and size distribution was validated using capillary electrophoresis and quantified using fluorimetry (PicoGreen, Thermo Fisher Scientific) and qPCR. Libraries were then normalized, pooled, and sequenced on an S4 flow cell by an Illumina NovaSeq 6000 using a 150-nucleotide, paired-end read strategy. The resulting FASTQ files were trimmed, aligned to the mouse reference genome (GRCm38), sorted, and counted using the Bulk RNAseq Analysis Pipeline from the Minnesota Supercomputing Institute's Collection of Hierarchical UMII/RIS Pipelines (v0.2.0 was used for 26-week-old data. v0.2.2 was used for the 10-week-old data).[43] Genes less than 300 bp are too small to be accurately captured in standard RNAseq library preparations, so they were discarded from all downstream analyses.

RNAseq Analyses—Differential gene expression analysis was performed using the edgeR package[44,45] (v3.30.3) in R (R Foundation for Statistical Computing v3.6.1). Genes shorter than 300 bp are too small to be accurately captured in standard RNAseq library preparations, so they were discarded from all analyses. All five brain regions were analyzed independently. Genes with fewer than 10 read counts across all 12 samples (3 genotypes, 4 mice per genotype) in each region were excluded. Genes with resulting FDR values less than or equal to 0.05 were considered significant. The UpSet plot was created using the UpSetR package[28] (v1.4.0) in R (v4.0.3). For motif bootstrapping, FIMO from MEME Suite[46] (v4.11.2) was utilized to identify the occurrence of each motif (CIC from Coffin et al,[30] ZKSCAN1 and RFX1 from JASPAR[47]) within 1 kb upstream of the transcriptional start site. Motif bootstrapping was performed as described by Coffin et al.[30] The frequency of differentially expressed genes for each RNA-seq dataset containing a motif was calculated as number of corrected genes with a motif divided by total number of corrected genes in

Author Manuscript Author Manuscript Author Manuscript Author Manuscript

each brain region. To examine significance of the observed frequency relative to random chance, we calculated the frequency of the motif within a random set of the same number of non-differentially expressed genes and randomly sampled 10,000 repetitions with each simulated repetition represented as a colored dot (color depicts brain region). P value was then computed as (r+1)/(n+1), where r is the number of repetitions where percentage of motifs in selected non-differentially expressed genes is greater than the percent of motifs in corrected genes and n is the total number of repetitions.[48,49] Plots are made in R (v4.0.3) with the ggplot2 package (v3.3.6).[50] Pathway analysis and dot plot creation was performed using the clusterProfiler package[31] (v3.16.1) in R (v4.0.3).

QUANTIFICATION AND STATISTICAL ANALYSIS

For all experiments, pre-hoc power calculations were performed in MATLAB (MathWorks) to determine the number of mice per genotype necessary to reach 80% power with an alpha level of 0.05. Historical data comparing *Atxn1*$^{2Q/2Q}$ mice to *Atxn1*$^{154Q/2Q}$ mice was used to estimate effect size (Cohen's d) for these power estimates. Aside from power calculations performed in MATLAB and the RNAseq analyses performed in R, all other statistical tests were performed using GraphPad Prism software (v9.0). All data were checked for normality and met assumptions for using parametric statistical tests. For multigroup comparisons, one-way or two-way ANOVAs were performed. When working with repeated-measures data, sphericity was not assumed; thus, a Geisser-Greenhouse correction was used. When ANOVA findings were significant, ($p<0.05$), the analysis was followed by multiple comparisons testing using Tukey's (all pairwise comparisons) or Dunnett's (comparisons back to one control group) correction for multiple comparisons. Survival analysis, plotted as Kaplan-Meyer curves, was assessed using log-rank Mantel-Cox and Gehan-Breslow-Wilcoxon tests. Western blots were quantified using ImageQuant TL software (Cytiva). For subcellular fractionation data, the nuclear proportion of expanded ATXN1 was calculated for each animal by dividing the intensity of the expanded ATXN1 nuclear band by the combined intensity of the nuclear band plus the cytoplasmic band. ATXN1 extractability was calculated by dividing the expanded ATXN1 band by the ATXN1[2Q] band for each animal. All data presented are shown as mean ± SEM. Significant results are denoted as * ($p<0.05$), ** ($p<0.01$), *** ($p<0.001$), and **** ($p<0.0001$). Complete statistical analysis details for all data analyzed in Prism are presented in Table S1.

Supplementary Material

Refer to Web version on PubMed Central for supplementary material.

ACKNOWLEDGEMENTS

This study was supported by NIH/NINDS grants R01NS022920 and R35NS127248. The authors thank the Genomics Center and Mouse Behavior Core at the University of Minnesota.

REFERENCES

1. Paulson HL, Shakkottai VG, Clark HB, and Orr HT (2017). Polyglutamine spinocerebellar ataxias-from genes to potential treatments. Nat. Rev. Neurosci 18, 613–626. 10.1038/nrn.2017.92. [PubMed: 28855740]

Author Manuscript Author Manuscript Author Manuscript Author Manuscript

2. Klement IA, Skinner PJ, Kaytor MD, Yi H, Hersch SM, Clark HB, Zoghbi HY, and Orr HT (1998). Ataxin-1 Nuclear Localization and Aggregation. Cell 95, 41–53. 10.1016/S0092-8674(00)81781-X. [PubMed: 9778246]

3. Peters MF, Nucifora FC, Kushi J, Seaman HC, Cooper JK, Herring WJ, Dawson VL, Dawson TM, and Ross CA (1999). Nuclear targeting of mutant huntingtin increases toxicity. Mol. Cell. Neurosci 14, 121–128. 10.1006/mcne.1999.0773. [PubMed: 10479410]

4. Nucifora FC, Ellerby LM, Wellington CL, Wood JD, Herring WJ, Sawa A, Hayden MR, Dawson VL, Dawson TM, and Ross CA (2003). Nuclear localization of a non-caspase truncation product of atrophin-1, with an expanded polyglutamine repeat, increases cellular toxicity. J. Biol. Chem 278, 13047–13055. 10.1074/jbc.M211224200. [PubMed: 12464607]

5. Bichelmeier U, Schmidt T, Hübener J, Boy J, Rüttiger L, Häbig K, Poths S, Bonin M, Knipper M, Schmidt WJ, et al. (2007). Nuclear localization of ataxin-3 is required for the manifestation of symptoms in SCA3: In vivo evidence. J. Neurosci 27, 7418–7428. 10.1523/JNEUROSCI.4540-06.2007. [PubMed: 17626202]

6. Sasaki H, Fukazawa T, Yanagihara T, Hamada T, Shima K, Matsumoto A, Hashimoto K, Ito N, Wakisaka A, and Tashiro K (1996). Clinical features and natural history of spinocerebellar ataxia type 1. Acta Neurol.Scand 93, 64–71. 10.1111/j.1600-0404.1996.tb00173. [PubMed: 8825276]

7. Genis D, Matilla T, Volpini V, Rosell J, Dávalos A, Ferrer I, Molins A, and Estivill X (1995). Clinical, neuropathologic, and genetic studies of a large spinocerebellar ataxia type 1 (SCA1) kindred: (CAG)n expansion and early premonitory signs and symptoms. Neurology 45, 24–30. 10.1212/WNL.45.1.24. [PubMed: 7824128]

8. Jacobi H, du Montcel ST, Bauer P, Giunti P, Cook A, Labrum R, Parkinson MH, Durr A, Brice A, Charles P, et al. (2015). Long-term disease progression in spinocerebellar ataxia types 1, 2, 3, and 6: A longitudinal cohort study. Lancet Neurol. 14, 1101–1108. 10.1016/S1474-4422(15)00202-1. [PubMed: 26377379]

9. Orengo JP, van der Heijden ME, Hao S, Tang J, Orr HT, and Zoghbi HY (2018). Motor neuron degeneration correlates with respiratory dysfunction in SCA1. DMM Dis. Model. Mech 11, 1–7. 10.1242/DMM.032623.

10. Tejwani L, and Lim J (2020). Pathogenic mechanisms underlying spinocerebellar ataxia type 1. Cell. Mol. Life Sci 77, 4015–4029. 10.1007/s00018-020-03520-z. [PubMed: 32306062]

11. Rüb U, Bürk K, Timmann D, den Dunnen W, Seidel K, Farrag K, Brunt E, Heinsen H, Egensperger R, Bornemann A, et al. (2012). Spinocerebellar ataxia type 1 (SCA1): New pathoanatomical and clinico-pathological insights. Neuropathol. Appl. Neurobiol 38, 665–680. 10.1111/j.1365-2990.2012.01259.x. [PubMed: 22309224]

12. Koscik TR, Sloat L, van der Plas E, Joers JM, Deelchand DK, Lenglet C, Öz G, and Nopoulos PC (2020). Brainstem and striatal volume changes are detectable in under 1 year and predict motor decline in spinocerebellar ataxia type 1. Brain Commun. 2, 1–13. 10.1093/braincomms/fcaa184.

13. Reetz K, Costa AS, Mirzazade S, Lehmann A, Juzek A, Rakowicz M, Boguslawska R, Schöls L, Linnemann C, Mariotti C, et al. (2013). Genotype-specific patterns of atrophy progression are more sensitive than clinical decline in SCA1, SCA3 and SCA6. Brain 136, 905–917. 10.1093/brain/aws369. [PubMed: 23423669]

14. Watase K, Weeber EJ, Xu B, Antalffy B, Yuva-Paylor L, Hashimoto K, Kano M, Atkinson R, Sun Y, Armstrong DL, et al. (2002). A long CAG repeat in the mouse Sca1 locus replicates SCA1 features and reveals the impact of protein solubility on selective neurodegeneration. Neuron 34, 905–919. 10.1016/S0896-6273(02)00733-X. [PubMed: 12086639]

15. Zoghbi HY, and Orr HT (1995). Spinocerebellar ataxia type 1. Semin. Cell Biol 6, 29–35. [PubMed: 7620119]

16. Brasted PJ, and Wise SP (2004). Comparison of learning-related neuronal activity in the dorsal premotor cortex and striatum. Eur. J. Neurosci 19, 721–740. 10.1111/j.0953-816X.2003.03181.x. [PubMed: 14984423]

17. Costa RM, Cohen D, and Nicolelis MAL (2004). Differential Corticostriatal Plasticity during Fast and Slow Motor Skill Learning in Mice Rui. Curr. Biol 14, 1124–1134. 10.1016/j. [PubMed: 15242609]

Author Manuscript Author Manuscript Author Manuscript Author Manuscript

18. Barnes TD, Kubota Y, Hu D, Jin DZ, and Graybiel AM (2005). Activity of striatal neurons reflects dynamic encoding and recoding of procedural memories. Nature 437, 1158–1161. 10.1038/nature04053. [PubMed: 16237445]

19. Yin HH, Mulcare SP, Hilário MRF, Clouse E, Holloway T, Davis MI, Hansson AC, Lovinger DM, and Costa RM (2009). Dynamic reorganization of striatal circuits during the acquisition and consolidation of a skill. Nat. Neurosci 12, 333–341. 10.1038/nn.2261. [PubMed: 19198605]

20. Girault J-A, and Nairn A (2021). DARPP-32 40 years later. Adv. Pharmacol, 67–87. [PubMed: 33706939]

21. Kovalenko M, Milnerwood A, Giordano J, Claire JS, Guide JR, Stromberg M, Gillis T, Sapp E, DiFiglia M, MacDonald ME, et al. (2018). HttQ111/+ Huntington's Disease Knock-in Mice Exhibit Brain Region-Specific Morphological Changes and Synaptic Dysfunction. J. Huntingtons. Dis 7, 17–33. 10.3233/JHD-170282. [PubMed: 29480209]

22. Van Dellen A, Welch J, Dixon RM, Cordery P, York D, Styles P, Blakemore C, and Hannan AJ (2000). N-Acetylaspartate and DARPP-32 levels decrease in the corpus striatum of Huntington's disease mice. Neuroreport 11, 3751–3757. 10.1097/00001756-200011270-00032. [PubMed: 11117485]

23. Surmeier DJ, Ding J, Day M, Wang Z, and Shen W (2007). D1 and D2 dopamine-receptor modulation of striatal glutamatergic signaling in striatal medium spiny neurons. Trends Neurosci. 30, 228–235. 10.1016/j.tins.2007.03.008. [PubMed: 17408758]

24. Bürk K, Globas C, Bösch S, Klockgether T, Zühlke C, Daum I, and Dichgans J (2003). Cognitive deficits in spinocerebellar ataxia type 1, 2, and 3. J. Neurol 250, 207–211. 10.1007/S00415-003-0976-5. [PubMed: 12574952]

25. Asher M, Rosa JG, Rainwater O, Duvick L, Bennyworth M, Lai RY, Kuo SH, and Cvetanovic M (2020). Cerebellar contribution to the cognitive alterations in SCA1: Evidence from mouse models. Hum. Mol. Genet 29, 117–131. 10.1093/hmg/ddz265. [PubMed: 31696233]

26. Illouz T, Madar R, Clague C, Griffioen KJ, Louzoun Y, and Okun E (2016). Unbiased classification of spatial strategies in the Barnes maze. Bioinformatics 32, 3314–3320. 10.1093/bioinformatics/btw376. [PubMed: 27378295]

27. Irwin S, Vandelft M, Pinchev D, Howell JL, Graczyk J, Orr HT, and Truant R (2005). RNA association and nucleocytoplasmic shuttling by ataxin-1. J. Cell Sci 118, 233–242. 10.1242/jcs.01611. [PubMed: 15615787]

28. Conway JR, Lex A, and Gehlenborg N (2017). UpSetR: An R package for the visualization of intersecting sets and their properties. Bioinformatics 33, 2938–2940. 10.1093/bioinformatics/btx364. [PubMed: 28645171]

29. Lam YC, Bowman AB, Jafar-Nejad P, Lim J, Richman R, Fryer JD, Hyun ED, Duvick LA, Orr HT, Botas J, et al. (2006). ATAXIN-1 Interacts with the Repressor Capicua in Its Native Complex to Cause SCA1 Neuropathology. Cell 127, 1335–1347. 10.1016/j.cell.2006.11.038. [PubMed: 17190598]

30. Coffin SL, Durham MA, Nitschke L, Xhako E, Brown AM, Revelli J-P, Villavicencio Gonzalez E, Lin T, Handler HP, Dai Y, et al. Disruption of the ATXN1-CIC complex reveals the roleof additional nuclear ATXN1 interactors in spinocerebellar ataxia type 1. Neuron.

31. Yu G, Wang LG, Han Y, and He QY (2012). ClusterProfiler: An R package for comparing biological themes among gene clusters. Omi. A J. Integr. Biol 16, 284–287. 10.1089/omi.2011.0118.

32. Friedrich J, Kordasiewicz HB, O'Callaghan B, Handler HP, Wagener C, Duvick L, Swayze EE, Rainwater O, Hofstra B, Benneyworth M, et al. (2018). Antisense oligonucleotide-mediated ataxin-1 reduction prolongs survival in SCA1 mice and reveals disease-associated transcriptome profiles. JCI insight 3, 1–17. 10.1172/jci.insight.123193.

33. Nitschke L, Coffin SL, Xhako E, El-Najjar DB, Orengo JP, Alcala E, Dai Y, Wan YW, Liu Z, Orr HT, et al. (2021). Modulation of ATXN1 S776 phosphorylation reveals the importance of allele-specific targeting in SCA1. JCI Insight 6, 1–15. 10.1172/JCI.INSIGHT.144955.

34. Cummings CJ, Reinstein E, Yaling S, Antalffy B, Jiang YH, Ciechanover A, Orr HT, Beaudet AL, and Zoghbi HY (1999). Mutation of the E6-AP ubiquitin ligase reduces nuclear inclusion

Author Manuscript Author Manuscript Author Manuscript Author Manuscript

frequency while accelerating polyglutamine-induced pathology in SCA1 mice. Neuron 24, 879–892. 10.1016/S0896-6273(00)81035-1. [PubMed: 10624951]

35. Driessen TM, Lee PJ, and Lim J (2018). Molecular pathway analysis towards understanding tissue vulnerability in spinocerebellar ataxia type 1. Elife, 1–32. 10.7554/eLife.39981.
36. Luttik K, Olmos V, Owens A, Khan A, Yun J, Driessen T, and Lim J (2022). Identifying Disease Signatures in the Spinocerebellar Ataxia Type 1 Mouse Cortex. Cells 11, 1–17. 10.3390/cells11172632.
37. Ingram M, Wozniak EAL, Duvick L, Yang R, Bergmann P, Carson R, O'Callaghan B, Zoghbi HY, Henzler C, and Orr HT (2016). Cerebellar Transcriptome Profiles of ATXN1 Transgenic Mice Reveal SCA1 Disease Progression and Protection Pathways. Neuron 89, 1194–1207. 10.1016/j.neuron.2016.02.011. [PubMed: 26948890]
38. Bushart DD, and Shakkottai VG (2019). Ion channel dysfunction in cerebellar ataxia. Neurosci. Lett 688, 41–48. 10.1016/j.neulet.2018.02.005. [PubMed: 29421541]
39. Yang H, Wang H, and Jaenisch R (2014). Generating genetically modified mice using CRISPR/Cas-mediated genome engineering. Nat. Protoc 9, 1956–1968. 10.1038/nprot.2014.134. [PubMed: 25058643]
40. Richardson CD, Ray GJ, DeWitt MA, Curie GL, and Corn JE (2016). Enhancing homology-directed genome editing by catalytically active and inactive CRISPR-Cas9 using asymmetric donor DNA. Nat. Biotechnol 34, 339–344. 10.1038/nbt.3481. [PubMed: 26789497]
41. Servadio A, Koshy B, Armstrong D, Antalffy B, Orr HT, and Zoghbi HY (1995). Expression analysis of the ataxin-1 protein in tissues from normal and spinocerebellar ataxia type 1 individuals. Nat. Genet 10, 94–98. 10.1038/ng0595-94. [PubMed: 7647801]
42. Pérez Ortiz JM, Mollema N, Toker N, Adamski CJ, O'Callaghan B, Duvick L, Friedrich J, Walters MA, Strasser J, Hawkinson JE, et al. (2018). Reduction of protein kinase A-mediated phosphorylation of ATXN1-S776 in Purkinje cells delays onset of Ataxia in a SCA1 mouse model. Neurobiol. Dis 116, 93–105. 10.1016/j.nbd.2018.05.002. [PubMed: 29758256]
43. Baller J, Kono T, Herman A, and Zhang Y (2019). ChURP: A lightweight CLI framework to enable novice users to analyze sequencing datasets in parallel. ACM Int. Conf. Proceeding Ser. 10.1145/3332186.3333156.
44. Robinson MD, McCarthy DJ, and Smyth GK (2009). edgeR: A Bioconductor package for differential expression analysis of digital gene expression data. Bioinformatics 26, 139–140. 10.1093/bioinformatics/btp616. [PubMed: 19910308]
45. McCarthy DJ, Chen Y, and Smyth GK (2012). Differential expression analysis of multifactor RNA-Seq experiments with respect to biological variation. Nucleic Acids Res. 40, 4288–4297. 10.1093/nar/gks042. [PubMed: 22287627]
46. Bailey TL, Johnson J, Grant CE, and Noble WS (2015). The MEME Suite. Nucleic Acids Res. 43, W39–W49. 10.1093/nar/gkv416. [PubMed: 25953851]
47. Mathelier A, Zhao X, Zhang AW, Parcy F, Worsley-Hunt R, Arenillas DJ, Buchman S, Chen CY, Chou A, Ienasescu H, et al. (2014). JASPAR 2014: An extensively expanded and updated open-access database of transcription factor binding profiles. Nucleic Acids Res. 42, 142–147. 10.1093/nar/gkt997.
48. Lavery LA, Ure K, Wan YW, Luo C, Trostle AJ, Wang W, Jin H, Lopez J, Lucero J, Durham MA, et al. (2020). Losing dnmt3a dependent methylation in inhibitory neurons impairs neural function by a mechanism impacting rett syndrome. Elife 9, 1–27. 10.7554/eLife.52981.
49. North BV, Curtis D, and Sham PC (2002). A Note on the Calculation of Empirical P Values from Monte Carlo Procedures. Am. J. Hum. Genet, 439–441. 10.1080/13518040701205365. [PubMed: 12111669]
50. Wickham H (2009). ggplot2: Elegant Graphics for Data Analysis (Springer) 10.1007/978-0-387-98141-3.

Author Manuscript Author Manuscript Author Manuscript Author Manuscript

Highlights

- An SCA1 knock-in mouse model with a mutated NLS in ATXN1-polyQ was generated
- NLS mutation mitigates ATXN1-polyQ-related lifespan, motor, and cognitive deficits.
- Gene expression alterations and molecular pathology differ across brain regions.
- Nuclear localization of ATXN1-polyQ is a critical aspect of SCA1 disease pathology.

Author Manuscript Author Manuscript Author Manuscript Author Manuscript

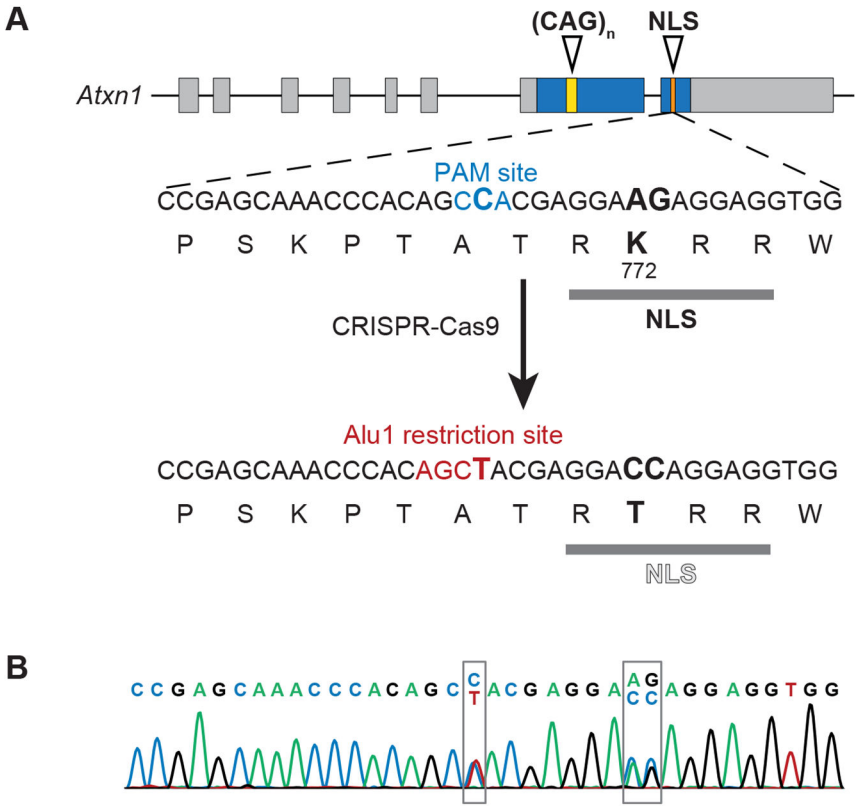

Figure 1. Generation of the *Atxn1*$^{175QK772T/2Q}$ mouse model

(A) CRISPR-Cas9 strategy used to create the *Atxn1*$^{175QK772T/2Q}$ mouse model. The K772T alteration in the nuclear localization sequence (NLS) of mouse ATXN1 protein was introduced by changing three nucleotides (bold) in the DNA sequence of the *Atxn1* gene. Two nucleotide alterations (AG → CC) changed a lysine codon at position 772 of the ATXN1 protein to a threonine codon (black). Another nucleotide alteration (C → T) ablated the PAM site (blue) and introduced an Alu1 restriction enzyme digest site (red).

(B) Sanger sequencing confirming the animals used for breeding were heterozygous for all three desired nucleotide changes.

Author Manuscript Author Manuscript Author Manuscript Author Manuscript

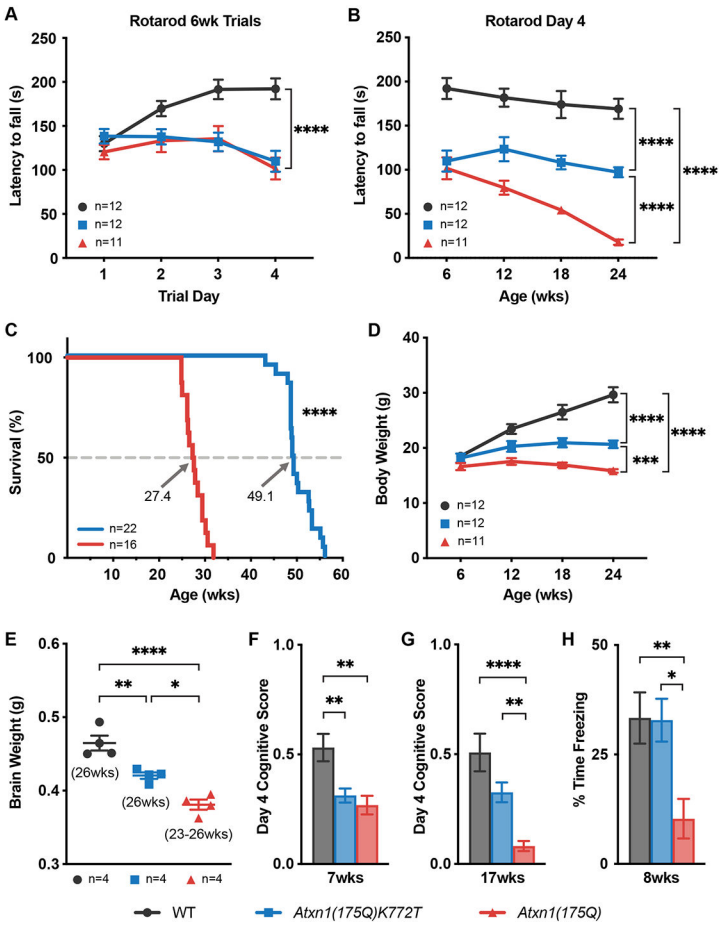

Figure 2. Key SCA1-like phenotypes

(A) Rotarod assessment learning among naïve mice across 4 trial days at 6 weeks of age.

(B) Rotarod performance on trial day 4 between 6 and 24 weeks of age.

(C) Mouse survival plotted as Kaplan-Meyer curves with median lifespan labeled for each genotype. For *Atxn1(175Q)K772T* n=22 and *Atxn1(175Q)* n=16. Statistical comparison of survival curves was performed using log-rank Mantel-Cox and Gehan-Breslow-Wilcoxon tests.

(D) Body weight measurements between 6 and 24 weeks of age.

(E) Brain weight measurements at 23-26 weeks of age. For all genotypes, n=4.

(F) Barnes maze assessment cognitive scores on trial day 4 at 7 weeks of age.

(G) Barnes maze assessment cognitive scores on trial day 4 at 17 weeks of age.

(H) Contextual fear conditioning assessment freezing time percentage among naïve mice at 8 weeks of age.

Data in (A), (B), and (D) are from the same cohort of mice. N values for each genotype are shown in the bottom of each bar in (F-H). Data in (A), (B), (D), (E), (F), (G), and (H) are represented as mean ± SEM. Two-way repeated measures ANOVAs with Tukey's post hoc test were performed for (A), (B), and (D). One-way ANOVA with Tukey's post hoc test was performed for (E-H). Statistical significance is depicted only for genotype comparisons at the last timepoint assessed in (A), (B), and (D). Significant results are denoted as * ($p<0.05$),

Author Manuscript Author Manuscript Author Manuscript Author Manuscript

** ($p<0.01$), *** ($p<0.001$), and **** ($p<0.0001$). Additional statistical analyses details are in Table S1.

See also Figure S1

Author Manuscript Author Manuscript Author Manuscript Author Manuscript

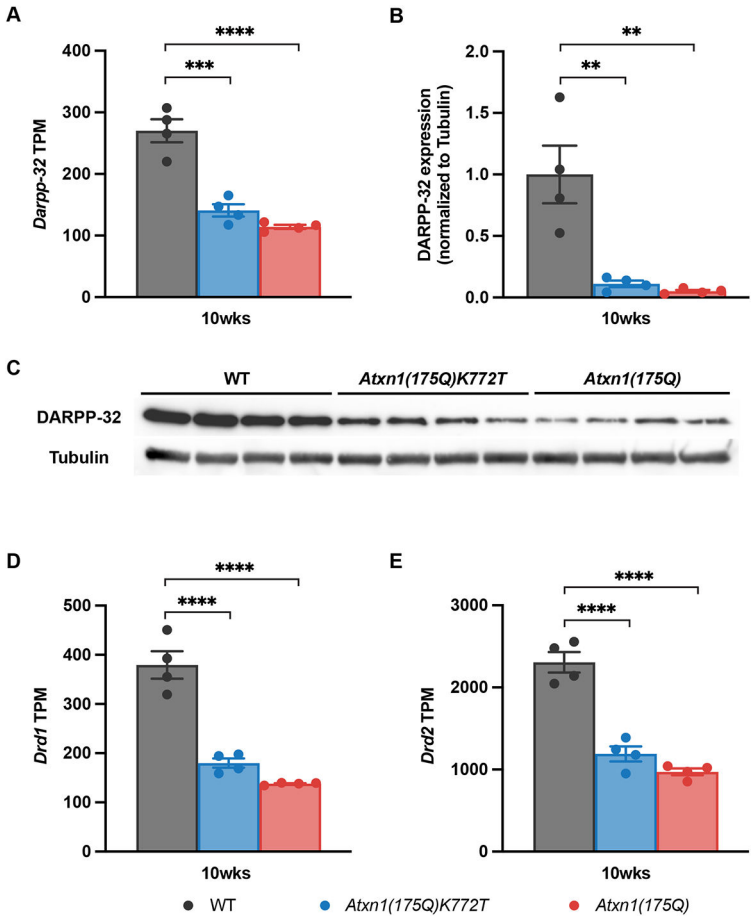

Figure 3. 10-week striatum expression

(A, D, and E) Expression of *Darpp-32* (A), *Drd1* (D), and *Drd2* (E) RNA (transcripts per million; TPM) in striatum at 10 weeks of age.

(B) DARPP-32 protein expression in striatum at 10 weeks of age. Quantification of Western blot shown in (C).

(C) Western blot used to quantify DARPP-32 protein expression in striatum at 10 weeks of age. Data in (A), (D), and (E) are from the same cohort of mice. N = 4 mice per genotype in all data shown. Data in (A), (B), (D) and (E) are represented as mean ± SEM and One-way ANOVA with Tukey's post hoc test was performed. Significant results are denoted as ** ($p<0.01$), *** ($p<0.001$), and **** ($p<0.0001$). Additional statistical analyses details are in Table S1.

Author Manuscript Author Manuscript Author Manuscript Author Manuscript

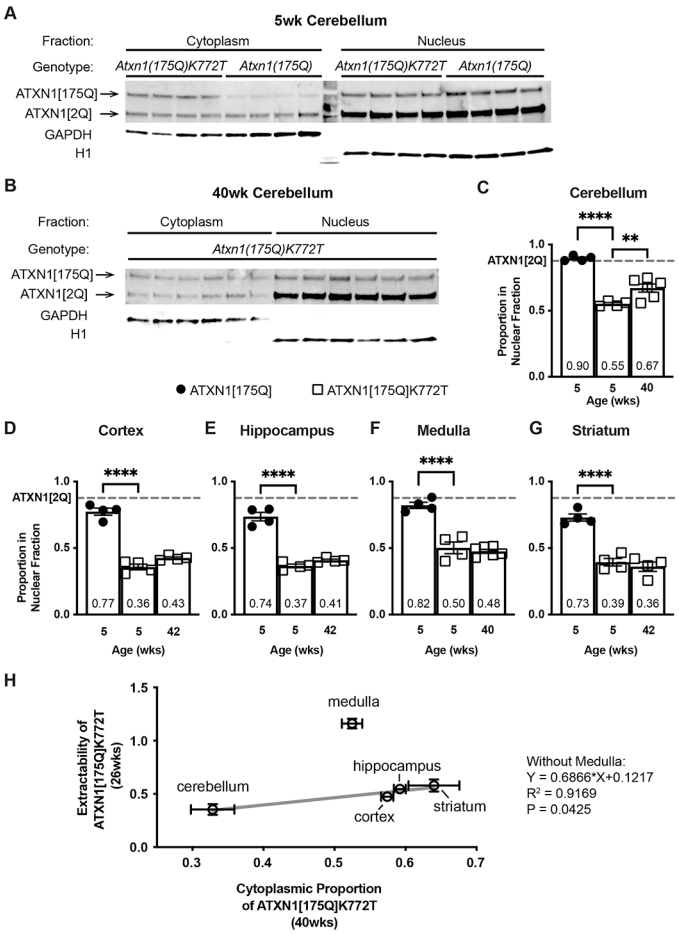

Figure 4. Subcellular fractionation

(A and B) Subcellular fractionation Western blot used to quantify nuclear proportion of expanded ATXN1 from cerebellar lysates in *Atxn1(175Q)* and *Atxn1(175Q)K772T* mice at 5 weeks of age (A) and in *Atxn1(175Q)K772T* mice at 40 weeks of age (B). GAPDH was used as a cytoplasmic marker and H1 was used as a nuclear marker to confirm purity of subcellular fractions. N=4 mice per genotype at 5 weeks of age (A) and n=6 mice at 40 weeks of age (B).

(C-G) Proportion of expanded ATXN1 in the nucleus of cells from the cerebellum (C), cerebral cortex (D), hippocampus (E), medulla (F), and striatum (G) at 5 weeks for *Atxn1(175Q)* and *Atxn1(175Q)K772T* mice and at 40-42 weeks for *Atxn1(175Q)K772T* mice. For all brain regions, n=4 mice per genotype at 5 weeks of age and n=4-6 mice at 40-42 weeks of age. Nuclear proportion of ATXN1 was determined by dividing the intensity of nuclear expanded ATXN1 bands by the intensity of expanded ATXN1 bands in the nucleus and cytoplasm combined for a given genotype at a given time. The dashed line represents the average nuclear proportion of ATXN1[2Q] protein product across the three assessments for a particular brain region.

(H) Relationship between extractability of ATXN1[175Q]K772T and proportion of ATXN1[175Q]K772T found in the cytoplasm for all brain regions assessed. Simple linear regression was performed excluding the medulla data.

Author Manuscript Author Manuscript Author Manuscript Author Manuscript

Data in (C-H) are represented as mean ± SEM. One-way ANOVAs with Dunnett's post hoc test relative to the nuclear proportion of ATXN1[175QK772T] at 5 weeks were performed for (C-G). Significant results are denoted as * ($p<0.05$), ** ($p<0.01$), *** ($p<0.001$), and **** ($p<0.0001$). Statistical analysis details are in Table S1.
See also Figure S2, S3, S4, and S5

Author Manuscript Author Manuscript Author Manuscript Author Manuscript

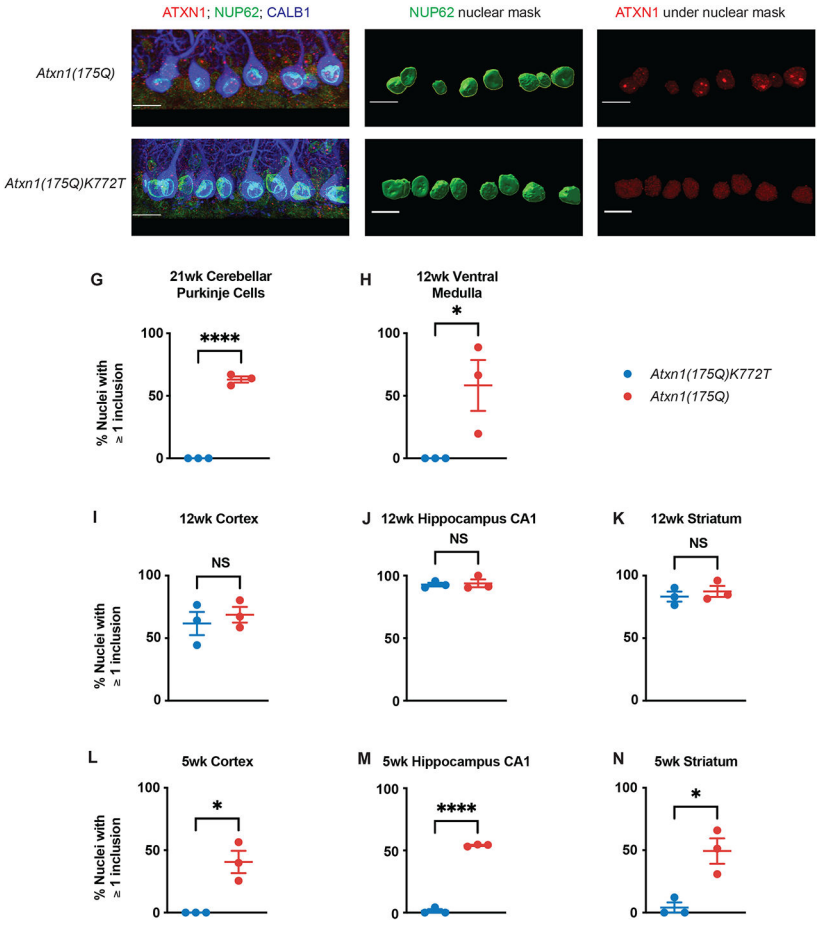

Figure 5. ATXN1 nuclear inclusions

(A and D) Immunofluorescent staining in cerebellar Purkinje cells of *Atxn1(175Q)* (A) and *Atxn1(175Q)K772T* (D) mice at 21 weeks of age. ATXN1 is shown in red, NUP62 is shown in green, and CALB1 is shown in blue.

(B and E) Nuclear mask generated by Imaris using NUP62 staining in Purkinje cells of *Atxn1(175Q)* (B) and *Atxn1(175Q)K772T* (E) mice at 21 weeks of age.

(C and F) ATXN1 staining under the nuclear mask in Purkinje cells of *Atxn1(175Q)* (C) and *Atxn1(175Q)K772T* (F) mice at 21 weeks of age.

(G-N) Percentage of nuclei analyzed with at least one ATXN1 inclusion present in *Atxn1(175Q)* and *Atxn1(175Q)K772T* cerebellar Purkinje cells at 21 weeks (G), ventral medulla at 12 weeks (H), cerebral cortex at 13 weeks (I), CA1 of the hippocampus at 12 weeks (J), and striatum at 12 weeks (K), cerebral cortex at 5 weeks (L), CA1 of the hippocampus at 5 weeks (M), striatum at 5 weeks (N). For all brain regions at all time points, n=3 mice per genotype. Data are represented as mean ± SEM. Unpaired two-tailed t tests were performed. Significant results are denoted as * ($p<0.05$), ** ($p<0.01$), *** ($p<0.001$), and **** ($p<0.0001$). Statistical analysis details are in Table S1.

See also Figure S6

Author Manuscript Author Manuscript Author Manuscript Author Manuscript

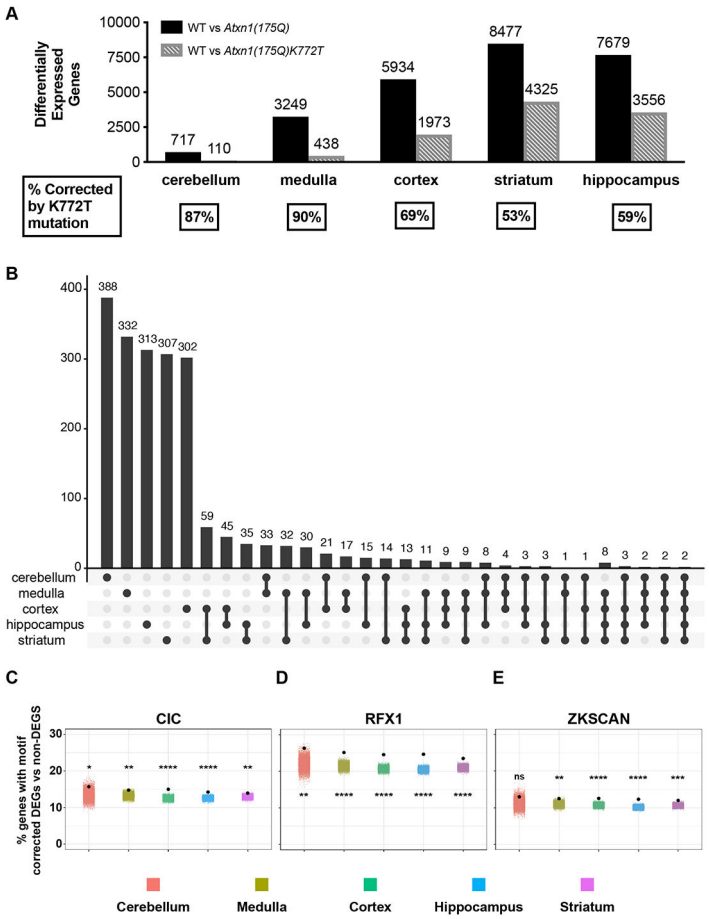

Figure 6. RNAseq analyses

(A) Significantly differentially expressed gene numbers between WT and *Atxn1(175Q)* mice (black) and between WT and *Atxn1(175Q)K772T* mice (gray) in cerebellum, medulla, cerebral cortex, striatum, and hippocampus tissue at 26 weeks of age. Genes that were significantly differentially expressed in the comparison between WT and *Atxn1(175Q)* mice and were not significantly differentially expressed in the comparison between WT and *Atxn1(175Q)K772T* mice were considered corrected by the K772T mutation. The percentage of genes corrected for each brain region is listed below the bar graph. For all genotypes, n=4 mice.

(B) Brain region(s) where the top 500 corrected genes (genes with the largest absolute value Log_2(Fold Change) in the comparison between WT and *Atxn1(175Q)* mice) from each region are found to be significantly differentially expressed.

(C-E) Jitter plots of motif enrichment among genes corrected by the NLS mutation relative to genes that are not significantly differentially expressed in the WT vs. *Atxn1(175Q)* comparison. Black dots indicate the percentage of corrected genes with a CIC (C), RFX1 (D), or ZKSCAN1 (E) motif within 1kb of the transcriptional start site for genes in each brain region. Colored jitter plot dots represent the percentage of non-differentially expressed genes with a given motif within 1kb of the transcriptional start site. Each colored jitter plot dot represents one of 10,000 random iterations selecting a set of genes the same size as the number of corrected genes in each brain region. P value was computed as (r+1)/(n+1) where

r is the number of repetitions where percent motifs in selected non-differentially expressed genes is greater than the percent of motifs or peaks in DEGs experimentally determined and n is the total number of repetitions.

Author Manuscript Author Manuscript Author Manuscript Author Manuscript

Author Manuscript Author Manuscript Author Manuscript Author Manuscript

Figure 7. Corrected Gene Pathway enrichment

Pathway analysis of the top 500 corrected genes from each brain region performed using the molecular function domain of the Gene Ontology database.

Author Manuscript Author Manuscript Author Manuscript Author Manuscript

KEY RESOURCES TABLE

REAGENT or RESOURCE
Antibodies
mouse monoclonal anti-Nucleoporin p62
guinea pig polyclonal anti-Calbindin D28k
rabbit polyclonal anti-Atxn1 12NQ
rabbit polyclonal anti-Atxn1 11750
rabbit polyclonal anti-Histone H1
mouse monoclonal anti-GAPDH
mouse monoclonal anti-Ubiquitin
rat monoclonal anti-DARPP-32
mouse monoclonal anti-alpha-Tubulin
anti-mouse polyclonal IgG Alexa 488
anti-guinea pig polyclonal IgG Alexa 647
anti-rabbit polyclonal IgG Cy3
anti-mouse IgG HRP
anti-rat IgG HRP
anti-rabbit IgG HRP
Chemicals, peptides, and recombinant proteins
TRIzol reagent
Phosphatase Inhibitor Cocktail 2
Phosphatase Inhibitor Cocktail 3
cOmplete Mini, EDTA-free Protease Inhibitor Cocktail
RNA*later* Stabilization Solution
ProLong Gold Antifade Mountant
SuperSignal West Pico PLUS
SuperSignal West Dura

Author Manuscript Author Manuscript Author Manuscript Author Manuscript

REAGENT or RESOURCE
Restore PLUS Western Blot Stripping Buffer
Alt-R HiFi Cas9 Nuclease V3
Alu1 Restriction Endonuclease
Critical commercial assays
NE-PER kit
Pierce BCA Protein Assay kit
Quant-iT RiboGreen assay kit
Quant-iT PicoGreen assay kit
Light Cycler 480 Probes Master kit
Deposited data
RNAseq FastQ files
RNAseq counts data and DEG analysis
Experimental models: Organisms/strains
Mouse: *C57BL/6*
Mouse: *C57BL/6 Atxn1*$^{2Q/175Q}$
Mouse: *C57BL/6 Atxn1*$^{2Q/175QK772T}$
Oligonucleotides
guide RNA: 5’-CGACCACCTCCTCTTCCTCG-3’
ssODN: 5’-AAAATAGGATTGCCTGCAGCACCCTTCCTCAGCAAAATAGAACCGAGCAAACCCACAGCtACGAGGAccAGGAGGTGGTCGGCGCCGGAGACCCGTAAACTGGAG
Primer *Atxn1* 175Q Forward: 5’-ACCTTCCAGTTCATTGGGTC-3’
Primer *Atxn1* 175Q Reverse: 5’-GCTCTGTGGAGAGCTGGA-3’
Primer *Atxn1* K772T Forward: 5’-GCCGTGTTCCAAACTCTCTG-3’
Primer *Atxn1* K772T Reverse: 5’-GGTCTCTACTTGCCCACGTTA-3’
Software and algorithms
Prism
Pipeline for UMII/RIS RNAseq Analysis
edgeR package
clusterProfiler package

Author Manuscript Author Manuscript Author Manuscript Author Manuscript

REAGENT or RESOURCE
UpSetR package
Imaris version 9.8
ANY-maze Video Tracking Software
Video Freeze
Barnes-maze unbiased strategy (BUNS) algorithm
TIDE
ICE Analysis
CRISP-ID
Custom Alt-R CRISPR-Cas9 guide RNA design tool
R
MATLAB
Fiji
ImageQuant TL